

# Discrimination between cyclic nucleotides in a cyclic nucleotide-gated ion channel

Received: 24 July 2022

Accepted: 24 February 2023

Published online: 27 March 2023

 Check for updates

Yangang Pan<sup>1</sup>, Emmi Pohjolainen<sup>2</sup>, Philipp A. M. Schmidpeter<sup>1</sup>,  
Andrea C. Vaiana<sup>1,2,4</sup>, Crina M. Nimigea<sup>1,3</sup>, Helmut Grubmüller<sup>2</sup> &  
Simon Scheuring<sup>1,3</sup> ✉

Cyclic nucleotide-gated ion channels are crucial in many physiological processes such as vision and pacemaking in the heart. SthK is a prokaryotic homolog with high sequence and structure similarities to hyperpolarization-activated and cyclic nucleotide-modulated and cyclic nucleotide-gated channels, especially at the level of the cyclic nucleotide binding domains (CNBDs). Functional measurements showed that cyclic adenosine monophosphate (cAMP) is a channel activator while cyclic guanosine monophosphate (cGMP) barely leads to pore opening. Here, using atomic force microscopy single-molecule force spectroscopy and force probe molecular dynamics simulations, we unravel quantitatively and at the atomic level how CNBDs discriminate between cyclic nucleotides. We find that cAMP binds to the SthK CNBD slightly stronger than cGMP and accesses a deep-bound state that a cGMP-bound CNBD cannot reach. We propose that the deep binding of cAMP is the discriminatory state that is essential for cAMP-dependent channel activation.

Cyclic nucleotide-gated (CNG) channels play important roles throughout the entire nervous system, particularly in the signal transduction of the retina and olfactory system<sup>1–4</sup>. They are regulated by cyclic nucleotides (cN), that is, cyclic adenosine monophosphate (cAMP) and cyclic guanosine monophosphate (cGMP), which bind to a specialized intracellular domain called the cyclic nucleotide-binding domain (CNBD). Accordingly, CNG channels are key in translating the chemical signal of the second messenger molecules cAMP and cGMP into an electrical response through a cN-binding-induced conformational change in the CNBD that modulates the opening of the channel gate in the pore domain allowing the flow of ions across cell membranes<sup>5</sup>.

CNG channels belong to the superfamily of voltage-gated cation channels—a group of membrane proteins that form tetramers—where each subunit consists of six transmembrane (TM) helices<sup>6</sup>. Helices S1 to S4 form the voltage sensor domain (VSD), and S5 to S6 form the pore domain, around the ion-conductive channel center. The signature feature of CNG channels is the CNBD, which is located at the C terminus and connected to the channel via a C-linker (CL) that mechanically

transmits conformational changes from the CNBD to the TM domain, thereby modulating opening and closing of the channel gate (Fig. 1a).

Due to their physiological importance, CNG channels, and the closely related hyperpolarization-activated and cyclic nucleotide-modulated (HCN) channels, have been studied extensively using genetic approaches and electrophysiology, and structurally using cryogenic electron microscopy (cryo-EM)<sup>7–10</sup>. SthK, a prokaryotic CNG homolog, was identified as a good structural and functional model with which to investigate the working mechanism of CNG channels (Fig. 1a,b). Electrophysiological single-channel recordings at depolarized membrane potentials (+100 mV) showed that cAMP triggers an open probability  $P_o$  of around 0.4, while the binding of cGMP led to only very rare channel openings,  $P_o$  around 0.001 (refs. 7,11). In agreement, high-speed atomic force microscopy (HS-AFM) showed reversible conformational changes of SthK when cAMP was replaced by cGMP and vice versa, where the cGMP-bound conformation resembled the resting apo state<sup>12</sup>. The X-ray structures of the cAMP- and cGMP-bound CNBD-CL protomers revealed that the CNBDs were similar, while conformational

<sup>1</sup>Department of Anesthesiology, Weill Cornell Medicine, New York, NY, USA. <sup>2</sup>Max Planck Institute for Multidisciplinary Sciences, Theoretical and Computational Biophysics Department, Goettingen, Germany. <sup>3</sup>Department of Physiology and Biophysics, Weill Cornell Medicine, New York, NY, USA.

<sup>4</sup>Present address: Institute of Biophysics, National Research Council, Palermo, Italy. ✉e-mail: [sis2019@med.cornell.edu](mailto:sis2019@med.cornell.edu)

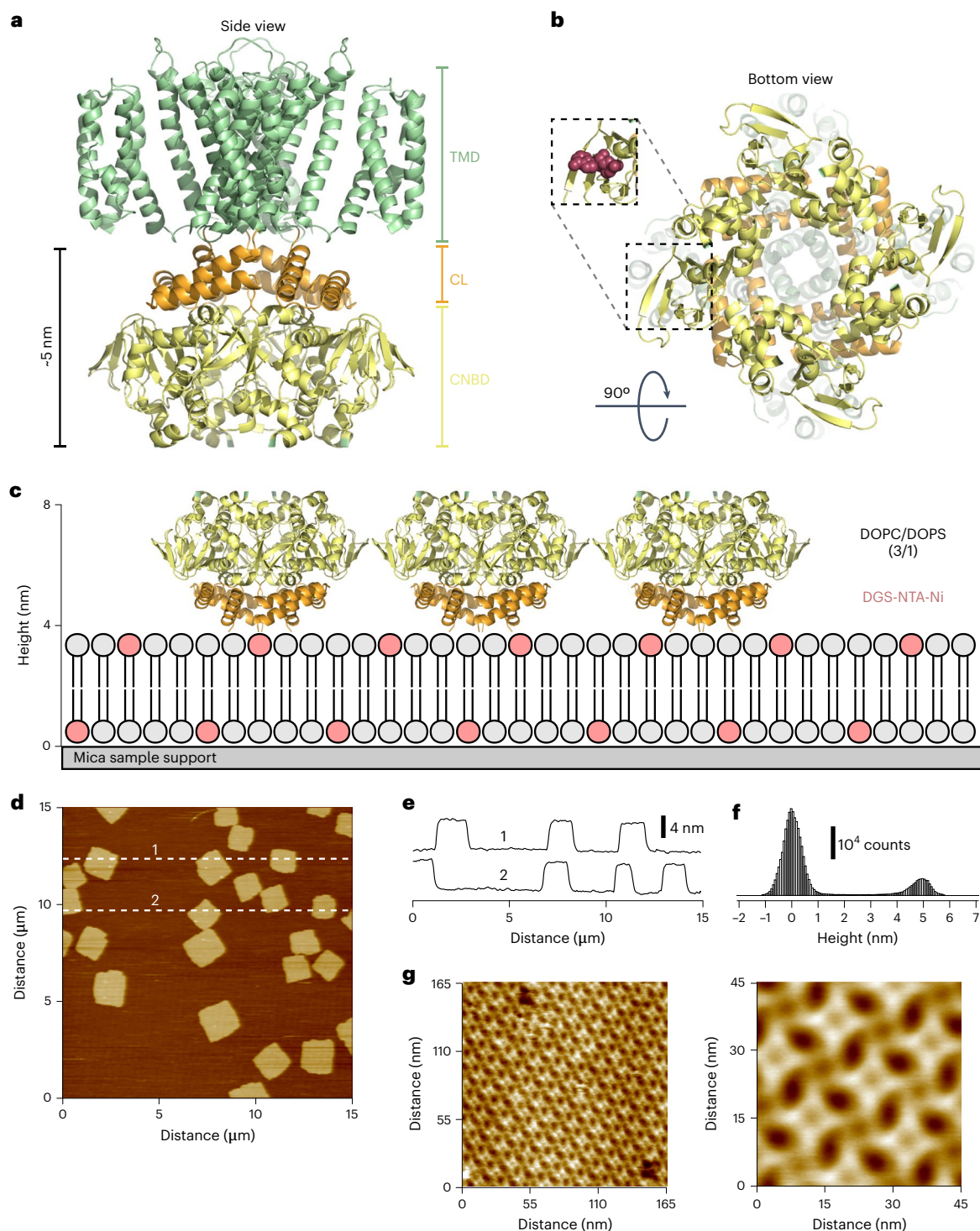


**Fig. 1 | 2D crystallization of SthK CL-CNBD.** **a**, Side view of the SthK channel structure (PDB 6CJQ) with transmembrane domain (TMD, green), intracellular CL domain (orange) and CNBD (yellow). **b**, Bottom view of the SthK channel onto the intracellular face. Inset, cyclic nucleotide binding site with bound cAMP (red). **c**, Schematic of His<sub>6</sub>-CL-CNBDs assembling on a DOPC/DOPS (3:1) membrane containing 20% Ni<sup>2+</sup>-NTA lipids (DGS-NTA-Ni, light pink). **d**, Overview AFM

topography of His<sub>6</sub>-CL-CNBD 2D crystals on a lipid bilayer containing Ni<sup>2+</sup>-NTA headgroups. **e**, Cross-sections of the 2D crystals along the dashed lines 1 and 2 in **d**. **f**, Height distribution histogram of all pixels in **d**. The membrane height level is set to 0 nm and the height of CNBD patches is measured as around 5 nm. **g**, High-resolution AFM images of a His<sub>6</sub>-CL-CNBD 2D crystal exposing the CNBDs to the solution (unit cell:  $a = b = 11$  nm,  $\gamma = 90^\circ$ ).

changes in the CL helices occurred. These changes related to the binding of cAMP and cGMP and resulted in differences in the tetramer assembly, where the cAMP-bound CNBD-CL tetramer was in an activated conformation while the cGMP-bound CNBD-CL tetramer was in a resting conformation<sup>13</sup>. Here we ask, how do the cAMP and cGMP

binding modes and energetics differ to yield distinct structural and functional readouts?

We investigated the differences of the interaction and binding strength of cAMP and cGMP with the CNBD on the single-molecule level using atomic force microscopy (AFM) single-molecule force

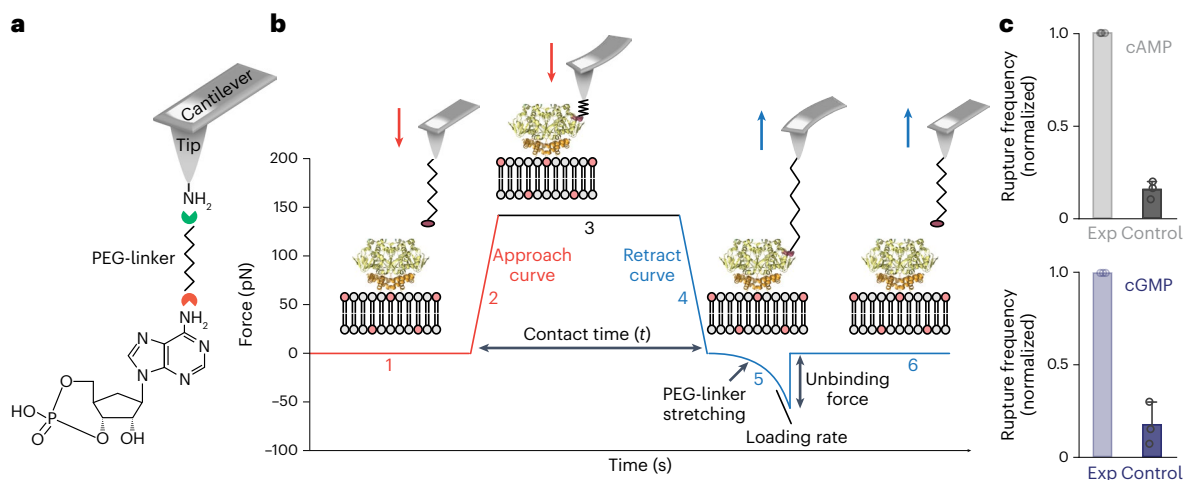


**Fig. 2 | Schematic of the experiment to probe the cN-CNBD interaction using AFM-SMFS. a**, Surface chemistry to tether cNs, here cAMP (chemical structure), to the AFM tip via a three-step protocol: first, amine groups are introduced to the inert silicon-nitride tip surface. Second, a PEG-linker is covalently coupled to the tip. Third, cAMP is coupled to the free end of the linker. **b**, Force measurement cycle: at a fixed lateral position, the deflection (force) of the cantilever is recorded as a function of the tip-sample distance. In the approaching period (red line) the deflection remains zero until the tip touches the surface (1). Upon further approach, the cantilever bends upward and a linearly increasing force is applied to the surface (2). The tip contacts the CNBD for a preset time at a preset force (3). Upon tip retraction (blue line) cantilever bending relaxes until

the cantilever reaches again its resting position (4). In case of a CNBD-cN bond formation, the tip surface attachment leads to a downward bending of the cantilever and stretching of the PEG-linker (5) until the CNBD-cN bond breaks (5, 6). The loading rate of force application on the bond and the unbinding force are the measurable extracted from each individual SMFS cycle. **c**, Specificity of AFM-SMFS measurements: for control, saturating concentrations, 2 mM cAMP or cGMP were injected into the fluid cell during cAMP-CNBD or cGMP-CNBD experiments (Exp), respectively. In the presence of soluble ligand, the cN-CNBD complex formation decreased by around 85%. The error bars indicate s.d. of the mean value.  $N = 3$  independent experiments for both cAMP and cGMP experiments.

spectroscopy (SMFS) and atomistic molecular dynamics simulations (MDS). AFM-SMFS enables detection and quantification of single molecular bonds in the pico-Newton range and provides insights into the dynamics of the recognition process<sup>14</sup>. We determined the rates of dissociation ( $k_{off}$ ) and association ( $k_{on}$ ) and distances to the unbinding transition energy barrier ( $x_{\beta}$ ) of cAMP- and cGMP binding with the CNBD. To gain atomic-level insights into the nucleotide binding modes and unbinding pathways, we performed force probe MDS, in silico experiments in which the cN is computationally pulled out of the CNBD binding pocket. The simulations were designed to mimic the experimental setup as closely as possible, and we focused on the structural and energetic determinants of the differences between cAMP and cGMP unbinding. With good agreement between experiment and simulation, we found that cAMP and cGMP bind in similar ways to the apo CNBD. However, only cAMP efficiently drives the CNBD into a deeper bound state.

## Results

### Surface density- and orientation-controlled CNBDs for SMFS

For SMFS experiments of a ligand-receptor pair, where the AFM tip is ligand-functionalized and the surface is decorated with the receptor, the ideal receptor immobilization should fulfill the following criteria: (1) the receptors are densely packed with well-defined receptor number per surface area, (2) the receptor binding pocket is facing towards the bulk and is well accessible for the ligand and (3) the ligand-receptor binding interaction is not influenced by other molecular determinants.

For this, we first optimized the surface immobilization of the CNBDs on supported lipid bilayers containing nickel-chelating lipids on freshly cleaved mica. Such nickel-lipid bilayers have been used for tethering soluble histidine-tagged proteins for AFM investigation<sup>15</sup>. We then supplemented the purified His<sub>6</sub>-CL-CNBD constructs onto the bilayers, allowing them to form NTA-Ni<sup>2+</sup>-His<sub>6</sub>-CL-CNBD complexes (Fig. 1c). In this case, the CNBD binding pockets are well-accessible to the bulk. Note, to get stable NTA-Ni<sup>2+</sup>-His<sub>6</sub>-CL-CNBD complexes,

we used bilayers containing a high percentage of nickel-lipid (20% DGS-NTA-Ni<sup>2+</sup>) and optimized the adsorption conditions by using low bulk protein concentration (0.05  $\mu$ M) and long incubation times. Together, this allowed the nickel-lipid and His<sub>6</sub>-tag to form stable polyvalent bonds<sup>16</sup>. AFM imaging demonstrated the successful His<sub>6</sub>-CL-CNBD immobilization and revealed that His<sub>6</sub>-CL-CNBD formed well-ordered square-shaped two-dimensional (2D) crystals on the lipid bilayer (Fig. 1d). Cross-section (Fig. 1e) and pixel height histogram (Fig. 1f) analyses showed that the protein layer had a thickness of around 5 nm, in excellent agreement with the dimensions of the CL-CNBD, as documented in previous cryo-EM and HS-AFM studies (Fig. 1a)<sup>7,12</sup>. Such large (around  $1.5 \times 1.5 \mu\text{m}^2$ ), square-shaped, flat and well-ordered CNBD 2D layers (Fig. 1d) allowed placement of the cN-functionalized tip (Fig. 2a) onto the CNBD protein region. High-resolution AFM images of the membrane-coupled His<sub>6</sub>-CL-CNBD 2D crystals revealed a tetrameric assembly of the construct with the typical windmill-like appearance of the exposed CNBDs (Fig. 1g), in agreement with structural studies of isolated CL-CNBDs<sup>17-19</sup>. The CNBD 2D crystal with unit cell dimension of  $a = b = 11 \text{ nm}$ ,  $\gamma = 90^\circ$  (area:  $121 \text{ nm}^2$ ) containing four CNBDs allowed us to calculate a precise binding-site surface density of  $0.03 \text{ binding sites nm}^{-2}$ .

The second step towards performing SMFS experiments was the functionalization of the AFM tip into a monomolecular cN biosensor with a coupling strategy that uses a heterobifunctional polyethylene glycol (PEG) linker between tip and cN (Fig. 2a)<sup>20</sup>. This protocol allows (1) fine-tuning of the ligand density on the AFM tip surface and therefore enables the detection of single-molecule interactions, (2) reduced interference of unspecific interactions by the chemical and physical properties of PEG and (3) selection of relevant force curves postacquisition through the identification of the characteristic PEG-linker stretching signature<sup>21</sup>. The cN-CNBD interaction is measured in force-distance cycles, where the unbinding force of the cN-CNBD complex is reported in the vertical distance between the maximal downward bending of the cantilever before bond breakage and the relaxed cantilever baseline

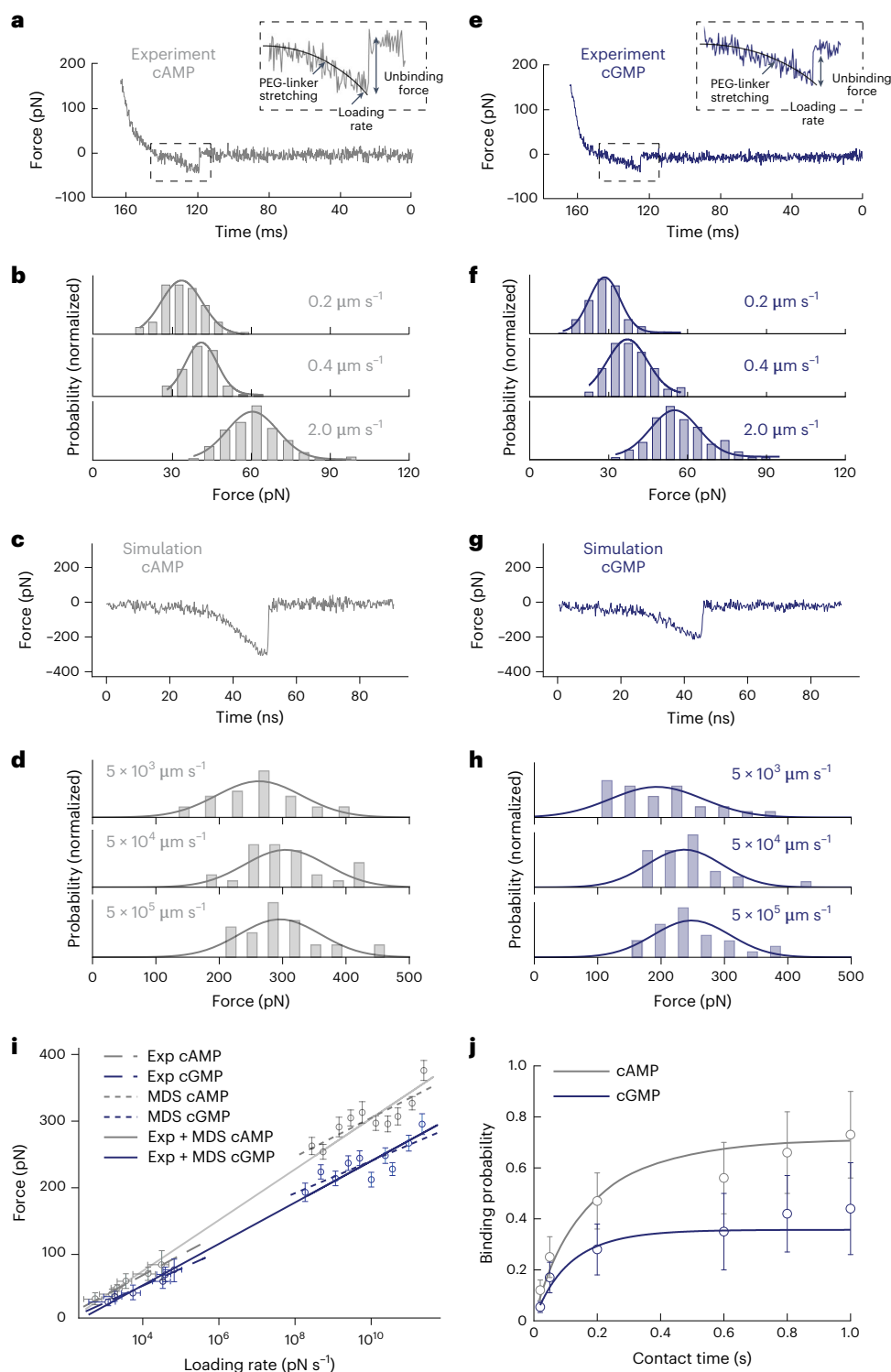


**Fig. 3 | Binding kinetics of cAMP-CNBD and cGMP-CNBD.** **a,e**, Representative force-distance curves of cAMP-CNBD (**a**) and cGMP-CNBD (**e**) unbinding events, respectively, recorded at  $0.4 \mu\text{m s}^{-1}$  pulling speed. **b,f**, Rupture force histograms at three different pulling speeds ( $0.2 \mu\text{m s}^{-1}$ ,  $0.4 \mu\text{m s}^{-1}$  and  $2.0 \mu\text{m s}^{-1}$ ) of cAMP-CNBD (**b**) and cGMP-CNBD (**f**) (lines: Gaussian fits). **c,g**, Representative simulation force curves of cAMP-CNBD (**c**) and cGMP-CNBD (**g**) unbinding events, respectively. **d,h**, Rupture force histograms from simulations at three different pulling speeds of cAMP-CNBD (**d**) and cGMP-CNBD (**h**) (lines: Gaussian fits). **i**, Dynamic force spectra of the most probable rupture forces of cAMP-CNBD and cGMP-CNBD complexes, respectively, versus logarithm of the loading

rate. To guide the eye, the lines show Bell-Evans model fits as indicated; equation (2). See Table 1 for detailed fit results of the experiment, the MDS and the combined data. The most probable rupture force (Gaussian peak) and error (full width at half maximum of the Gaussian peak) at each loading rate was determined through Gaussian fitting of the corresponding histogram ( $N = 851$  datapoints for cAMP, and  $N = 991$  datapoints for cGMP). **j**, Binding probability (bond formation per total number of experimental cycles) of cAMP and cGMP to the CNBD, respectively, as a function of cN-CNBD contact time (lines: probabilistic binding frequency model fits; equation (3)). Each datapoint represents the mean binding probability  $\pm$  s.d. (error bar) ( $N = 3$  independent experiments).

**Table 1 | cN–CNBD binding kinetics**

Method (Bell–Evans fit)	cN	$k_{\text{off}}$ ( $1\text{ s}^{-1}$ )	$x_{\beta}$ (nm)	$K_{\text{a}(2\text{D})}$ ( $\text{nm}^2$ )	$k_{\text{on}(2\text{D})}$ ( $\text{nm}^2\text{ s}^{-1}$ )	$K_{\text{a}}$	$k_{\text{on}}$ ( $1\text{ s}^{-1}$ )
AFM-SMFS+MDS	cAMP	$6.5 \pm 3.0$	$0.25 \pm 0.01$	—	—	—	—
AFM-SMFS+MDS	cGMP	$13.9 \pm 6.9$	$0.31 \pm 0.01$	—	—	—	—
AFM-SMFS	cAMP	$4.2 \pm 1.1$	$0.30 \pm 0.03$	$10.4 \pm 1.3$	$43.8 \pm 16.9$	$0.31 \pm 0.04$	$1.3 \pm 0.5$
AFM-SMFS	cGMP	$7.7 \pm 1.5$	$0.37 \pm 0.03$	$4.9 \pm 0.5$	$37.8 \pm 9.7$	$0.15 \pm 0.02$	$1.2 \pm 0.3$
MDS	cAMP	$0.03 \pm 0.14$	$0.32 \pm 0.07$	—	—	—	—
MDS	cGMP	$0.11 \pm 0.58$	$0.39 \pm 0.10$	—	—	—	—

$K_{\text{a}}$  and  $k_{\text{on}}$  have been calculated knowing the binding-site density  $m_{\text{t}} = 0.03$  binding sites  $\text{nm}^{-2}$  (see 2D crystal analysis in Fig. 1g).

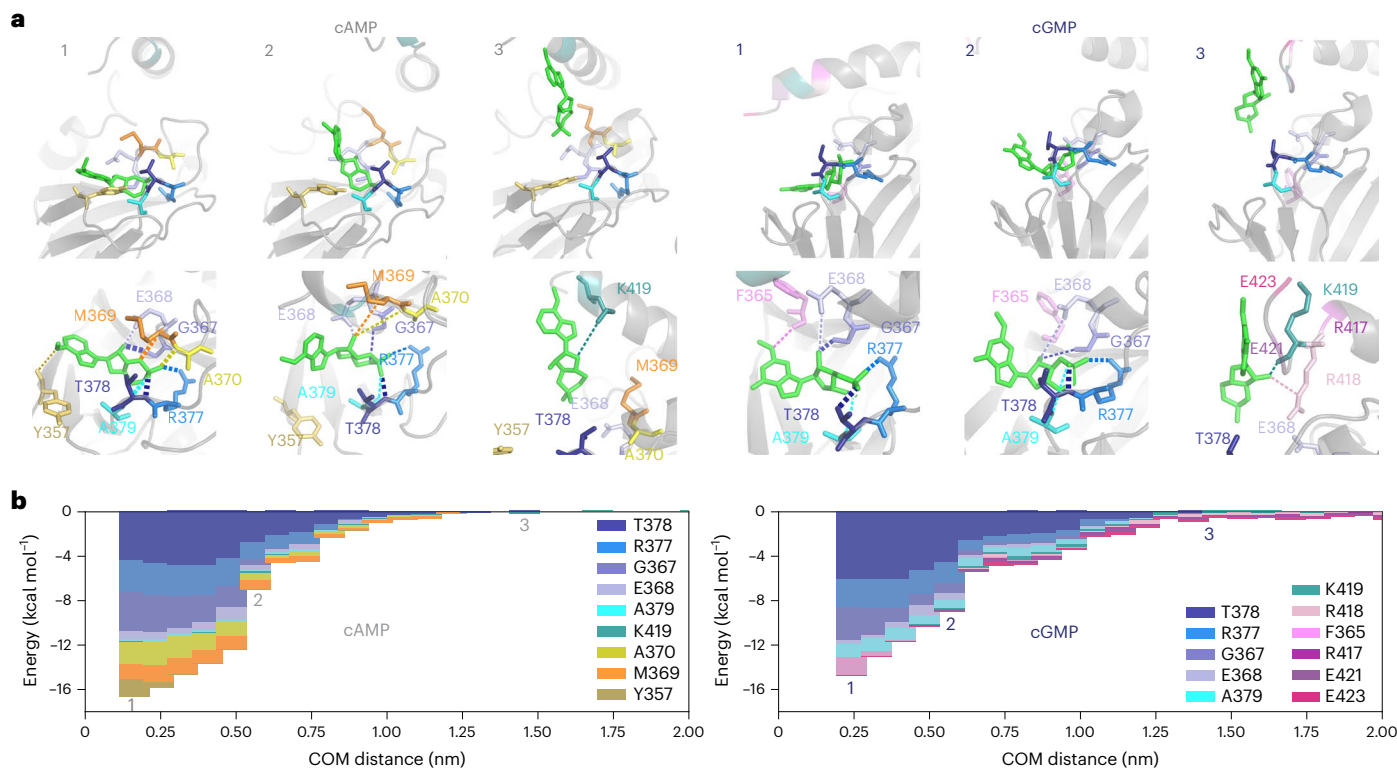


**Fig. 4 | H-bond interactions between CNBD and cNs. a**, From left to right: Top, representative simulation snapshots at increasing COM (geometric average of all cN atoms) separation in states 1, 2 and 3 along the unbinding pathway for the cAMP–CNBD (left) and cGMP–CNBD (right) complexes. cN is shown in green, the PEG-linker is omitted for clarity. Protein residues with highest contributions to the H-bond energies (defined as constituting 95% of the total integrated H-bond energy along the enforced unbinding) are shown colored, residues in the

pocket and on the C-helix (top) are shown in color and licorice mode. Bottom, corresponding close-up views showing H-bonds as dashed lines with three different line thicknesses representing the interaction strength (strong greater than  $3.5\text{ kcal mol}^{-1}$ ; intermediate  $1.7\text{--}3.5\text{ kcal mol}^{-1}$  and weak  $0.1\text{--}1.7\text{ kcal mol}^{-1}$  interactions). **b**, Energy contributions of residues as a function of cN-to-pocket COM separation distance for cAMP (left) and cGMP (right). Colored as the residues in the structural snapshots.

(steps 5 to 6; Fig. 2b). To assess the specificity of the cN–CNBD complex rupture measurements, we supplemented, as controls, the bulk with saturating (2 mM) cNs: in conditions where the surface-bound CNBDs can bind soluble cNs from the bulk, we found a decrease in rupture events of around 85% (Fig. 2c). The force probe MDS were set up in such a way as to mimic the AFM-SMFS experiments as closely as possible (Methods).

#### Bond strength of cN–CNBD interactions and binding kinetics

To quantitatively characterize the interaction kinetics as well as the unbinding pathways between cNs and CNBD, a large number ( $n > 10,000$ ) of force-distance cycles were recorded at various pulling speeds. The loading rates were extracted from the slope of the adhesive peak before rupture (Fig. 3a,e), ranging from  $10^2$  to  $10^5\text{ pN s}^{-1}$  in the

AFM-SMFS experiments, and from  $10^8$  to  $10^{11}\text{ pN s}^{-1}$  in the force probe MDS. In AFM-SMFS experiments, force-distance curves were acquired after a short cN–CNBD contact time of 0.02 s (step 3; Fig. 2b). The stretching of the PEG-linker, documented by a force-extension trace of around 10 nm in length before rupture in force-distance curves, was used as a molecular fingerprint for specific single-molecule events (Fig. 3a,e), further confirmed by the decrease in the frequency of binding events after supplementing the bulk with 2 mM cNs (Fig. 2c). For both, experiments (Fig. 3a,e) and simulations (Fig. 3c,g), two quantities are extracted from every single force curve: loading rate and unbinding force. The bond rupture forces at various loading rates were binned into unbinding force histograms from experiments (Fig. 3b,f) and simulations (Fig. 3d,h). The most probable rupture force at each loading rate was determined through Gaussian fitting the corresponding histogram (lines;

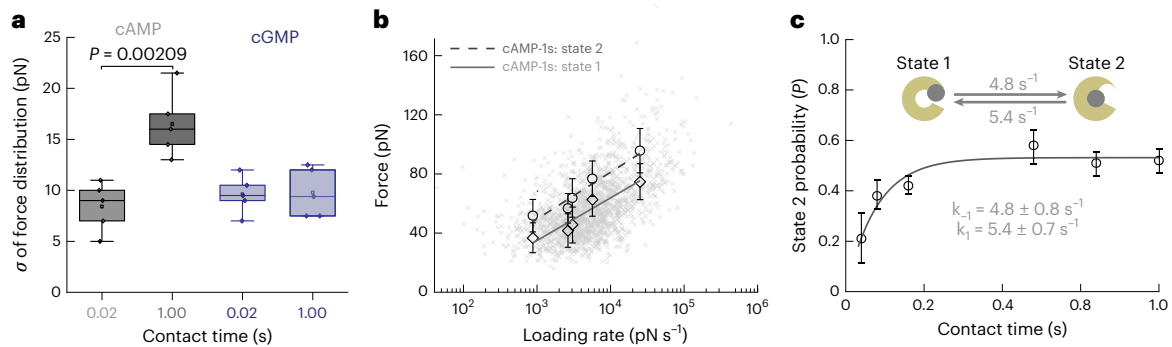


**Fig. 5 | A deep cAMP binding site after extended cAMP-CNBD bond formation.**

**a**, Force distribution ( $\sigma$ ) of cAMP-CNBD (left) and cGMP-CNBD (right) complexes after 0.02 s and 1.00 s bond formation contact times. The rupture force distribution after 1.00 s contact time is about twofold wider for cAMP ( $P = 0.00209$ ), but not for cGMP. Box, 25th–75th percentiles; square in the box, mean value; line in the box, median value. Top line, maximum value; bottom line, minimum value ( $N = 6$ ).  $P$  values were determined by two-sample  $t$ -test in Origin. **b**, Dynamic force spectrum and Bell–Evans model fits (lines) of the most probable rupture forces of cAMP-CNBD after 1.00 s bond formation time. Gray crosses, individual datapoints ( $N = 1,898$ ). Gray line, fit for state 1

bond (lower force distributions). Dashed line, fit for the state 2 bond (higher force distributions). The most probable rupture force (Gaussian peak) and error (full width at half maximum of the Gaussian peak) at each loading rate was determined through Gaussian fitting of the corresponding histogram (Extended Data Fig. 2b). **c**, Probability of occurrence of state 2 binding events as a function of cAMP-CNBD bond formation time. Gray line, fit of equation (1) to extract the reaction kinetics of state 2 bond formation. The state 2 probability was estimated from dividing the events under the second Gaussian fit by the total number of events and error bar is the full width at half maximum of the second peak at each contact time (total datapoints for all histograms,  $N = 1,917$ ; Extended Data Fig. 2f).

Fig. 3b,d,f,h). Pooling the data into a dynamic force spectrum revealed that the rupture forces of both cAMP-CNBD and cGMP-CNBD complexes increased linearly with the logarithm of the loading rate (Fig. 3i). Fitting the dynamic force spectra for cN-CNBD unbinding using the Bell–Evans model (equation (2); Methods)<sup>22</sup> allowed us to extract the dissociation constant ( $k_{\text{off}}$ ) and the distance to the unbinding barrier from the bound-state free energy minimum ( $x_{\beta}$ ). Note that, in both the experiments and simulations, cAMP binds more strongly than cGMP to the CNBD (Fig. 3i), and Bell–Evans fitting of experiment and simulation showed similar trends regarding  $k_{\text{off}}$  and  $x_{\beta}$  (dashed lines; Fig. 3i). However, the large dynamic range covered when merging the experimental and simulation data should define the kinetic parameters better. Therefore, we performed joint fitting of the experimental and simulation data and found that  $k_{\text{off}}$  of cGMP-CNBD was about twofold higher than that of cAMP-CNBD, that is, cAMP binds around twofold more strongly in the CNBD than cGMP. Also,  $x_{\beta}$  of cAMP-CNBD is around 20% shorter than that of cGMP-CNBD, indicating that cAMP is bound more tightly in the CNBD (Table 1). But can these rather minor differences alone explain the different action of the two cNs on channel function?

To gain further insights into the cAMP-CNBD and cGMP-CNBD complexes, we next characterized their 2D binding affinity. For this, we performed experiments to monitor the formation of cN-CNBD complexes during approach-retract cycles after varying predefined contact times ( $t$ ) during which the cN is presented to the binding pockets (step 3; Fig. 2b). As expected, the binding frequency ( $P$ ) increased with increasing contact time for both cNs, tending to plateau after around 0.4 s exposure (Fig. 3j). The association constant is determined by fitting the experimental data with the probabilistic model (equation (4); Methods)<sup>23</sup>,  $K_{\text{a}(2\text{D})}$  for cAMP was twofold higher than that of cGMP (Table 1). Knowing  $K_{\text{a}(2\text{D})}$  and  $k_{\text{off}}$ , the 2D-on-rates  $k_{\text{on}(2\text{D})}$  can be calculated following  $k_{\text{on}(2\text{D})} = K_{\text{a}(2\text{D})}k_{\text{off}}$ . In addition, knowing the binding-site density  $m_r$  (Fig. 1g), we can calculate the  $K_{\text{a}}$  for individual binding sites using  $K_{\text{a}} = K_{\text{a}(2\text{D})}m_r$ . Knowing  $K_{\text{a}}$  and  $k_{\text{off}}$  of individual binding sites, also the molecular on rate  $k_{\text{on}}$  can be calculated using  $k_{\text{on}} = K_{\text{a}}k_{\text{off}}$ . Provided that  $k_{\text{off}}$  of cGMP is about twofold higher than that of cAMP and  $K_{\text{a}}$  is twofold higher for cAMP than for cGMP, the on-rates of the two cNs are very similar (Table 1). We also measured the binding kinetics between the CNBD and cNs in bulk by performing microscale thermophoresis (MST) experiments. Two binding curves were detected for cAMP-CNBD measurements, the first with a  $K_{\text{D}}$  of  $0.4 \pm 0.5 \mu\text{M}$ , and the second with

a  $K_{\text{D}}$  of  $1.6 \pm 1.1 \mu\text{M}$  (Extended Data Fig. 1a,b). The  $K_{\text{D}}$  value of cGMP-CNBD was  $3.3 \pm 1.8 \mu\text{M}$  (Extended Data Fig. 1c,d). These results are in good agreement with the affinities of SthK full-length channels in amphipol that were determined as  $0.6 \mu\text{M}$  for cAMP and  $2.7 \mu\text{M}$  for cGMP<sup>11</sup>. While these bulk experiments show the same trends as our SMFS experiments, they cannot be compared directly since our SMFS measurements are performed on single-molecule CNBDs that are bound to a 2D membrane surface as in a native situation.

However, can the twofold higher association constant,  $K_{\text{a}}$ , and twofold lower dissociation constant,  $k_{\text{off}}$ , of cAMP explain that cAMP evokes increased activation of SthK by around three orders of magnitude as compared with cGMP?

### Structural basis of cNs unbinding kinetics differences

The good agreement between the AFM-SMFS and MDS force spectra motivated us to analyze the unbinding pathways of cAMP and cGMP from the CNBD from a structural perspective. Indeed, while AFM-SMFS allowed us to derive the  $k_{\text{on}}$  and  $K_{\text{a}}$ , MDS can provide us with a structural picture of the unbinding pathway. This approach seems justified as the experimental and simulation unbinding forces merge well in combined dynamic force spectra and thus likely report the same unbinding pathway and barrier. Thus, we analyzed all hydrogen bond interactions (Methods) along the dominant unbinding pathways identified in our atomistic force probe simulations (Fig. 4). From the set of force probe MDS with smallest loading rate of around  $10^6 \text{ pN s}^{-1}$ , we characterized the bound state and intermediates along the unbinding pathway structurally as well as in terms of interaction strength.

The force probe MDS trajectories (snapshots in Fig. 4a, top) allowed us to identify the most important residues that are involved in H-bond formation with the cNs in the binding pocket and along the unbinding pathway (Fig. 4a, bottom) and measure their strengths, that is, length and orientation (Fig. 4b). This analysis highlights similarities and differences between cAMP and cGMP binding. H-bond interaction energies with cAMP are larger than with cGMP, in agreement with, and explaining, the higher binding affinity of the CNBD for cAMP than for cGMP (Fig. 4b). This is especially pronounced at very short, less than 0.5 nm, center-of-mass (COM) separation distances, that is, deep inside the binding pocket. This finding is also in agreement with the shorter distance to the unbinding barrier from the free energy minimum,  $x_{\beta}$ , for cAMP-CNBD than for cGMP-CNBD reported by both

experiment and simulation (Table 1). Key residues (Fig. 4a, bottom) are: T378, R377, G367, E368 and A379 for both cAMP and cGMP in the bound state at COM separation less than 0.5 nm (state 1, where ‘state’ stands for cN location within a given COM separation range; Fig. 4b). In addition, cAMP interacts with A370, M369 and Y357, whereas cGMP interacts with F365. In state 2, at COM separation greater than 0.5 nm, the common core interactions are preserved but weakened. In state 3, at COM separation greater than 1.5 nm, transient interactions with the C-helix are seen, mainly with residue K419 for cAMP and residues K419, R417, R418, E421 and E423 for cGMP. We consider these interactions an outer binding pocket that might be crucial early during binding and explored transiently during unbinding, where it may lead to rebinding into deeper pockets. Not much difference (in energies) is seen for the shared interactions with residues T378, R377, G367 and E368. Rather, the stronger interactions seen for cAMP in the deep binding pocket are due largely to residues A370, M369 and Y357, which are not detected for cGMP. At corresponding short distances, cGMP interacts with F365, which is not observed for cAMP.

Of the above-mentioned interactions, the first to rupture and of similar strengths are with residues Y357 (cAMP only) and F365 (cGMP only) (Fig. 4a, bottom). Interactions of cAMP with M369 and A370 are longer-range, and not observed for cGMP. The exclusive interactions with Y357 (cAMP) and F365 (cGMP), as well as these longer-range interactions of cAMP with M369 and A370, are clear structural differences in the cN-binding modes that could explain the observed difference in the unbinding forces. Indeed, close inspection of the simulation trajectories revealed that, although the conformation of the binding pocket in state 1 is almost identical for cAMP and cGMP, cAMP forms a H-bond with Y357 between the amide group at position 6 and the backbone of Y357, and H-bonding to M369 and A370 occurs from the phosphate group. In the case of cGMP, which instead has a carboxyl group at position 6, interactions with F365 occur via its amide group at position 2, on the opposite side of the nucleotide plane. These different interaction modes of the cNs (cAMP-Y375 versus cGMP-F365) geometrically impose a slightly different orientation of the two cNs within the binding pocket. For cGMP, this moves the phosphate further away from residues M369 and A370, and these interactions are lost. At larger ligand-to-binding pocket distance, transient hydrogen bond interactions with the residues in the C-helix (residue numbers greater than 400) are observed. While both cAMP and cGMP show interactions with K419, we observed cGMP interactions with C-helix residues R417, R418, E421 and E423 (Fig. 4a, bottom).

### A stronger binding mode of cAMP–CNBD complexes only

The MDS structural analysis indicated that H-bond interaction energies with cAMP are substantially larger than with cGMP, at very short, less than 0.5 nm, COM separation distances; that is, cAMP could bind deeper inside the binding pocket than cGMP. Therefore, we extended our experimental matrix to evaluate whether the cNs would reach a different bound state if we allowed them to bind for longer. Thus, we allowed the cAMP-functionalized tip to interact with the CNBDs for different contact periods (as in the experiments in Fig. 3j), but now analyzing the rupture force distributions of the cN–CNBD complexes. Analyzing first simply the width of the rupture force distributions after 1.00 s as compared with after 0.02 s contact time (Fig. 5a, gray) indicated that the cAMP unbinding indeed changed with bond-formation duration (Extended Data Fig. 2a,b). Thus, we reasoned that cAMP–CNBD complexes had more than one binding state after extended bond formation time, as the distributions after short binding time followed theoretical predictions (Extended Data Fig. 3). This behavior was consistent across the various pulling speeds (Extended Data Fig. 2b). Such bimodal unbinding force distributions for different binding states have been observed for other membrane proteins such as the glucagon receptor or the serotonin transporter<sup>24,25</sup>. Following, we plotted the most probable unbinding forces of state 1 and state 2 bonds after 1 s

**Table 2 | State1 and state2 cAMP–CNBD unbinding kinetics**

cAMP	$k_{\text{off}}$ (1s <sup>-1</sup> )	$x_{\beta}$ (nm)	$k_1$ (1s <sup>-1</sup> )	$k_{-1}$ (1s <sup>-1</sup> )
20 ms bond formation time	4.2±1.1	0.30±0.03	—	—
1,000 ms bond formation time: state1 bond	5.2±3.3	0.33±0.06	—	—
1,000 ms bond formation time: state2 bond	2.1±1.4	0.30±0.05	5.4±0.7 <sup>a</sup>	4.8±0.8 <sup>a</sup>

<sup>a</sup>Rate constants of the interchange between state1 and state2 bonds.

bond formation for each loading rate in a dynamic force spectrum and analyzed them using the Bell–Evans model (equation (2)) to extract the kinetic parameters (Fig. 5b). To test whether the broadening of the unbinding force distribution was indeed due to a second binding mode and not due to the simultaneous rupture of several bonds (Extended Data Fig. 4), we turned to a Markovian sequence model (equation (5); Methods)<sup>26</sup>, which has been used widely to test for multibond ruptures<sup>27,28</sup>. We found that the measured dynamic force spectra of cAMP did not agree with the Markovian model for simultaneous dual bond rupture (Extended Data Fig. 5). Additionally, the broadening of the unbinding force distribution was found only for cAMP and not for cGMP (Fig. 5a), corroborating the assignment of the high force bond to a secondary, deeper binding mode.

Next, we investigated how the occurrence of state 2 bonds increased with bond formation time. Whereas after 0.02 s bond formation time the unbinding force distributions were fitted by only one Gaussian (Fig. 3b), we found that the occurrence of the state 2 cAMP–CNBD bond increased gradually with increasing bond formation times (Extended Data Fig. 2f). Thus, we could follow the temporal progression of cAMP entering the deeper binding mode. For this, the force distribution for each contact period was fitted by bimodal Gaussian fits, and the probability ( $p$ ) of state 2 bond formation was estimated by dividing the events under the second Gaussian fit by the total number of events (Fig. 5c). The population of state 2 bonds increased from undetectable at 0.02 s, to around 21% at 0.05 s and to around 51% at 1.00 s. Thus, plotting the state 2 bond state probability as a function of bond formation time described the dynamics to enter the deep binding mode, and could be fitted as a forward and reverse reaction using equation (1) (Fig. 5c, line):

$$p = \frac{k_1}{k_{-1} + k_1} \left( 1 - \frac{1}{e^{(k_{-1} + k_1)t}} \right) \quad (1)$$

where  $t$  is the bond formation time, and  $k_{-1}$  and  $k_1$  are the reverse and forward rate constants for cAMP entering the deeper binding mode in the CNBD,  $4.8 \pm 0.8 \text{ s}^{-1}$  and  $5.4 \pm 0.7 \text{ s}^{-1}$ , respectively.

The Bell–Evans analysis of the dynamic force spectra (Fig. 5b) revealed that the cAMP–CNBD complex kinetics of binding state 1 after 1.00 s bond formation time (continuous) are similar to those after 0.02 s contact time, while binding state 2 (dashed) has a dissociation rate that is around 2.5-fold lower (Table 2). From a structural perspective, cAMP binding might induce or allow a conformational change in the CNBD leading to a tightening of the cN-binding pocket<sup>7</sup>. Our results lead us to hypothesize that binding state 2 corresponds to an activated cAMP–CNBD, and that a bond formation time of around 0.2 s was needed to fully populate state 2 (Fig. 5c). In parallel, we compared the force distributions of cGMP–CNBD complexes after 0.02 s and 1.00 s bond formation time and could not detect a tighter bound state (Fig. 5a, blue). In electrophysiology single-channel recordings, cGMP is a poor agonist, leading to an open probability around 1,000-fold lower than that of cAMP, and in HS-AFM imaging the SthK CNBD was in a resting state (similar to the apo state) in presence of cGMP<sup>7</sup>. Thus, only cAMP engaged into a deeper state 2 binding mode, which is likely the state

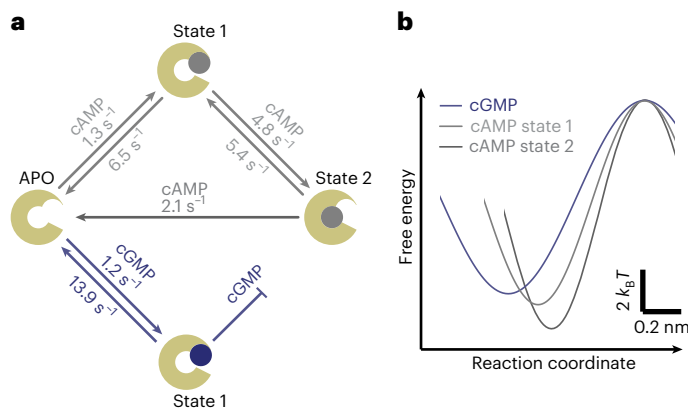


**Fig. 6 | Kinetic model of cAMP and cGMP binding to the SthK CNBD.** **a**, cAMP has an off-rate around twofold lower than that of cGMP, but very similar on-rates to bind in state 1. However, cAMP can exchange state 1 binding with a deeper bound state 2 that is inaccessible to cGMP. We propose that state 2 binding relates to a state that can activate the channel. **b**, Sketch of the energy landscapes of the cGMP and the two states of cAMP binding from the parameters provided in Supplementary Table 1 derived through the DHS model.

that leads to the marked functional differences between cAMP and cGMP. Remarkably, our results underline that extensive AFM-SMFS experiments at varying pulling velocities and ligand exposure times allow detection of agonist-induced conformational changes.

## Discussion

Electrophysiology and HS-AFM showed that cAMP and cGMP binding to the SthK CNBD resulted in different functional and structural responses on the full-length channel level<sup>7,12</sup>. Thus, the CNBD binding pocket must be able to discriminate between the two similar ligands. Here, we characterized the kinetics and interactions of cAMP and cGMP binding to the CNBD to deepen our understanding of ligand discrimination. We probed the binding/unbinding kinetics of cN–CNBD complexes using AFM-SMFS and atomistic MDS.

Our AFM-SMFS experiments incorporated (1) knowledge of the precise receptors density, (2) control of the orientation of the receptor binding pockets and (3) isolation of the ligand-receptor binding interaction from other molecular determinants. In addition, during the experiments, we controlled and varied (4) pulling speed and (5) contact time between the ligand-functionalized tip and the receptor-modified surface. A possible shortcoming of the AFM-SMFS experiments is that we must attach the cN to a linker to pull it out of the CNBD binding pocket. In both cases, cAMP and cGMP, the linker is attached to the amine group of the purine ring. From cN-bound CNBD structures<sup>13</sup>, we know that the phosphate group of the cNs lies deep in the binding pocket and the purine ring faces the gate. Also, the X-ray structures revealed that both cNs were in their elongated anti conformer in the binding pocket<sup>13</sup>. For these reasons, we would expect that the linker attachment allows a native-like vectorial pull of the cNs out of the binding pocket, but we cannot exclude that the linker attachment alters the binding kinetics or that the specific binding to the amine group in cAMP versus cGMP influenced the unbinding forces.

Our MDS forced unbinding experiments were equally meticulously designed, (1) pulling the cNs out of binding pockets in a direction identical to the experiment, (2) out of a tetrameric CNBD that was (3) oriented and immobilized by four harmonic potentials mimicking the four His-tags in the experiments, using (4) an atomistic model of the PEG-linker and (5) pulled by a harmonic potential with the nominal spring constant of the experimental cantilevers.

Altogether, AFM-SMFS and MDS agreed well and extended each other's dynamic range, such that the data could be merged, and

complemented each other regarding the kinetic data (AFM-SMFS) and structural interpretation (MDS). This allowed us to analyze unbinding pathways and energetics in atomistic detail. Analysis of cN–CNBD bonds following short (0.02 s) bond formation showed that the dissociation rate of cAMP from the CNBD was around twofold smaller than that of cGMP, 6.5 s<sup>-1</sup> versus 13.9 s<sup>-1</sup>. 2D binding kinetics AFM-SMFS experiments revealed that the 2D association constant of cAMP was only around twofold higher than that of cGMP, 0.31 versus 0.15 (Table 1); thus, the on-rates come out as very similar. Our atomistic MDS revealed specific H-bonds of cAMP in the binding pocket with residues M369 and A370 as the main determinant of its higher binding affinity.

The structural analysis from MDS suggested that cAMP could bind deeper inside the binding pocket than cGMP. Therefore, we further explored the possibility of several binding modes. Indeed, in the AFM-SMFS experiments the ligands were allowed to bind the receptor for only short times (0.02 s), whereas the simulations started from equilibrated structures. Thus, we allowed the cNs to bind for up to 1.00 s in experiments, and indeed detected a second, deeper binding state of cAMP to the CNBD that had a lower dissociation rate of around 2 s<sup>-1</sup> (compared with around 6 s<sup>-1</sup> after 0.02 s bond formation, Table 2). A similar behavior has been reported by single-molecule fluorescence measurements of HCN channels where cAMP could bind with varying dwell times<sup>29</sup>. Note that, in our study, as an advantage of AFM-SMFS, not only could the two different binding states be detected, but their interchange rates could also be determined ( $k_1 = 5.4 \text{ s}^{-1}$  and  $k_{-1} = 4.8 \text{ s}^{-1}$ ) (Fig. 6a). This finding suggests that a conformational transition in the CNBD, after around 0.2 s, brings cAMP (but not cGMP) into a deeper binding mode, potentially corresponding to a fully activated state. This time constant is in good agreement with functional measurements, which suggested that (1) the SthK functional response to cAMP exposure can occur within few hundred milliseconds<sup>30</sup>, and (2) only cAMP can activate the channel<sup>21</sup>. To extract the free energy profiles, our dynamic spectra were fitted using the DHS model<sup>31</sup>. We found that unbinding the cAMP–CNBD complex in state 2 had the highest energy barrier, at around 11  $k_B T$ , while unbinding the cGMP–CNBD complex had the lowest energy barrier, at around 9  $k_B T$  (Extended Data Fig. 6b and Supplementary Table 1). In addition to the free energy values, the DHS fit also yielded values for  $k_{\text{off}}$  and  $x_\beta$  (Supplementary Table 1). Comparison with the values derived from the Bell–Evans fit (Table 1) showed a similar trend and provided an estimate for the uncertainty of these values due to the model choice.

Our MDS results suggest that the CNBD binding pocket could discriminate between cAMP and cGMP through H-bonding to either Y357 (cAMP) or F365 (cGMP) leading to the formation of strong interactions of cAMP with the phosphate groups on the other side of the pocket with M369 and A370, which are inaccessible to cGMP. Interestingly, compared with SthK, the corresponding Y and F in the binding pocket are swapped in CNGA1 and CNGA3 channels, where cGMP is an agonist and cAMP is a poor agonist with low affinity (Extended Data Fig. 6)<sup>32,33</sup>, suggesting that these residues play a crucial role in ligand selectivity (cAMP versus cGMP) in CNG channels. Further studies are needed to explore this hypothesis.

Differential activation by cAMP and cGMP is a common feature of CNG and HCN channel isoforms. However, due to their highly conserved structure and pronounced sequence homology, a molecular explanation for the differential activation of these channels is still elusive. Our results here provide a potential mechanism. Minimal amino acid differences between isoforms are sufficient to alter the atomic environment of the ligand binding pocket allowing either cAMP or cGMP to enter the deep-bound state, which seems to be essential to induce large-scale conformational changes for channel gating.

## Online content

Any methods, additional references, Nature Portfolio reporting summaries, source data, extended data, supplementary information,

acknowledgements, peer review information; details of author contributions and competing interests; and statements of data and code availability are available at <https://doi.org/10.1038/s41594-023-00955-3>.

## References

1. Kaupp, U. B. & Seifert, R. Cyclic nucleotide-gated ion channels. *Physiol. Rev.* **82**, 769–824 (2002).
2. Craven, K. B. & Zagotta, W. N. CNG and HCN channels: two peas, one pod. *Annu. Rev. Physiol.* **68**, 375–401 (2006).
3. Robinson, R. B. & Siegelbaum, S. A. Hyperpolarization-activated cation currents: from molecules to physiological function. *Annu. Rev. Physiol.* **65**, 453–480 (2003).
4. Biel, M., Wahl-Schott, C., Michalakakis, S. & Zong, X. Hyperpolarization-activated cation channels: from genes to function. *Physiol. Rev.* **89**, 847–885 (2009).
5. James, Z. M. & Zagotta, W. N. Structural insights into the mechanisms of CNBD channel function. *J. Gen. Physiol.* **150**, 225–244 (2017).
6. Yu, F. H., Yarov-Yarovoy, V., Gutman, G. A. & Catterall, W. A. Overview of molecular relationships in the voltage-gated ion channel superfamily. *Pharmacol. Rev.* **57**, 387–395 (2005).
7. Rheinberger, J., Gao, X., Schmidpeter, P. A. M. & Nimigean, C. M. Ligand discrimination and gating in cyclic nucleotide-gated ion channels from apo and partial agonist-bound cryo-EM structures. *eLife* **7**, e39775 (2018).
8. Lee, C.-H. & MacKinnon, R. Structures of the human HCN1 hyperpolarization-activated channel. *Cell* **168**, 111–120.e111 (2017).
9. Saponaro, A. et al. Gating movements and ion permeation in HCN4 pacemaker channels. *Mol. Cell* **81**, 2929–2943.e2926 (2021).
10. Li, M. et al. Structure of a eukaryotic cyclic-nucleotide-gated channel. *Nature* **542**, 60–65 (2017).
11. Schmidpeter, P. A. M., Gao, X., Uphadyay, V., Rheinberger, J. & Nimigean, C. M. Ligand binding and activation properties of the purified bacterial cyclic nucleotide-gated channel SthK. *J. Gen. Physiol.* **150**, 821–834 (2018).
12. Marchesi, A. et al. An iris diaphragm mechanism to gate a cyclic nucleotide-gated ion channel. *Nat. Commun.* **9**, 3978 (2018).
13. Kesters, D. et al. Structure of the SthK carboxy-terminal region reveals a gating mechanism for cyclic nucleotide-modulated ion channels. *PLoS ONE* **10**, e0116369 (2015).
14. Florin, E. L., Moy, V. T. & Gaub, H. E. Adhesion forces between individual ligand-receptor pairs. *Science* **264**, 415 (1994).
15. Thess, A. et al. Specific orientation and two-dimensional crystallization of the proteasome at metal-chelating lipid interfaces. *J. Biol. Chem.* **277**, 36321–36328 (2002).
16. Nye, J. A. & Groves, J. T. Kinetic control of histidine-tagged protein surface density on supported lipid bilayers. *Langmuir* **24**, 4145–4149 (2008).
17. Lolicato, M. et al. Tetramerization dynamics of C-terminal domain underlies isoform-specific cAMP gating in hyperpolarization-activated cyclic nucleotide-gated channels. *J. Biol. Chem.* **286**, 44811–44820 (2011).
18. Zagotta, W. N. et al. Structural basis for modulation and agonist specificity of HCN pacemaker channels. *Nature* **425**, 200–205 (2003).
19. Lolicato, M. et al. Cyclic dinucleotides bind the C-linker of HCN4 to control channel cAMP responsiveness. *Nat. Chem. Biol.* **10**, 457–462 (2014).
20. Ebner, A. et al. A new, simple method for linking of antibodies to atomic force microscopy tips. *Bioconjug. Chem.* **18**, 1176–1184 (2007).
21. Baumgartner, W. et al. Cadherin interaction probed by atomic force microscopy. *Proc. Natl Acad. Sci. USA* **97**, 4005–4010 (2000).
22. Evans, E. & Ritchie, K. Dynamic strength of molecular adhesion bonds. *Biophys. J.* **72**, 1541–1555 (1997).
23. Huang, J. et al. The kinetics of two-dimensional TCR and pMHC interactions determine T-cell responsiveness. *Nature* **464**, 932–936 (2010).
24. Lo Giudice, C., Zhang, H., Wu, B. & Alsteens, D. Mechanochemical activation of class-B G-protein-coupled receptor upon peptide-ligand binding. *Nano Lett.* **20**, 5575–5582 (2020).
25. Zhu, R. et al. Allosterically linked binding sites in serotonin transporter revealed by single molecule force spectroscopy. *Front. Mol. Biosci.* **7**, 99 (2020).
26. Williams, P. M. Analytical descriptions of dynamic force spectroscopy: behaviour of multiple connections. *Anal. Chim. Acta* **479**, 107–115 (2003).
27. Rankl, C. et al. Multiple receptors involved in human rhinovirus attachment to live cells. *Proc. Natl Acad. Sci. USA* **105**, 17778–17783 (2008).
28. Sulchek, T. A. et al. Dynamic force spectroscopy of parallel individual Mucin1–antibody bonds. *Proc. Natl Acad. Sci. USA* **102**, 16638–16643 (2005).
29. White, D. S. et al. cAMP binding to closed pacemaker ion channels is non-cooperative. *Nature* **595**, 606–610 (2021).
30. Schmidpeter, P. A. M., Rheinberger, J. & Nimigean, C. M. Prolyl isomerization controls activation kinetics of a cyclic nucleotide-gated ion channel. *Nat. Commun.* **11**, 6401 (2020).
31. Dudko, O. K., Hummer, G. & Szabo, A. Intrinsic rates and activation free energies from single-molecule pulling experiments. *Phys. Rev. Lett.* **96**, 108101 (2006).
32. Aman, T. K., Gordon, S. E. & Zagotta, W. N. Regulation of CNGA1 channel gating by interactions with the membrane. *J. Biol. Chem.* **291**, 9939–9947 (2016).
33. Brady, J. D. et al. Interplay between PIP3 and calmodulin regulation of olfactory cyclic nucleotide-gated channels. *Proc. Natl Acad. Sci. USA* **103**, 15635–15640 (2006).

**Publisher's note** Springer Nature remains neutral with regard to jurisdictional claims in published maps and institutional affiliations.

Springer Nature or its licensor (e.g. a society or other partner) holds exclusive rights to this article under a publishing agreement with the author(s) or other rightsholder(s); author self-archiving of the accepted manuscript version of this article is solely governed by the terms of such publishing agreement and applicable law.

© The Author(s), under exclusive licence to Springer Nature America, Inc. 2023

## Methods

### Cloning, expression and purification of the His<sub>6</sub>-CL-CNBD construct

The isolated CL-CNBD domain of SthK (UniProtKB, G0GA88, residues 226–423) was cloned into pET11a (Novagen) using *Nde*I and *Bam*HI (NEB) restriction sites. The sequence Met-His<sub>6</sub>-Gly<sub>2</sub>-Ser-Gly was fused to the gene at the N terminus as purification tag. Sequencing using T7 primers confirmed the correct cloning. For protein expression, *Escherichia coli* BL21 (DE3) (NEB) transformed with pET 11a-SthK (226–423) was grown in Luria-Bertani medium at 37 °C. At optical density at 600 nm wavelength of 0.6, cells were transferred to 18 °C, a final concentration of 1 mM isopropylthiogalactoside was added and cells were further grown overnight. Cells were collected by centrifugation (7,500g, 4 °C, 10 min), resuspended in breaking buffer (50 mM Tris, pH 7.8 at room temperature, 100 mM KCl, 200 μM cAMP) supplemented with PMSF (85 μg ml<sup>-1</sup>), leupeptin/pepstatin (0.95/1.4 μg ml<sup>-1</sup>), DNase I (1 mg), lysozyme (1 mg) (all from MilliporeSigma), and cOmplete ULTRA mini protease inhibitor (Roche) and broken by sonication. Cell debris and insoluble components were pelleted by centrifugation (37,500g, 4 °C, 45 min), the supernatant was filtered (0.22 μm) and loaded onto a pre-equilibrated (20 mM Hepes, 100 mM KCl, 50 mM imidazole, pH 7.8, 150 μM cAMP) 5 ml HiTrap chelating HP Ni<sup>2+</sup> column (GE Life Sciences) at a flow rate of 1.5 ml min<sup>-1</sup> at room temperature. The column was washed with 15 column volumes of buffer and tightly bound protein was eluted (20 mM Hepes, 100 mM KCl, 300 mM imidazole, pH 7.8, 150 μM cAMP). His<sub>6</sub>-CL-CNBD protein was concentrated to around 1 ml using a 10 kDa cut-off Amicon ultraconcentrator (MilliporeSigma) and further purified by gel filtration (Superdex 200 16/600, GE Life Sciences, in 20 mM Hepes, 100 mM KCl, pH 7.4, flow rate 1 ml min<sup>-1</sup>, 4 °C). The peak corresponding to tetrameric His<sub>6</sub>-CL-CNBD was collected and concentrated (10 kDa cut-off) to 2.35 mM as determined by absorbance using an extinction coefficient of  $\epsilon_{280} = 8,940 \text{ M}^{-1} \text{ cm}^{-1}$  for the monomeric construct. Protein was flash-frozen in liquid nitrogen and stored at -80 °C for further use.

### Lipid preparation

All lipids (dioleoylphosphatidyl-choline (DOPC), dioleoylphosphatidyl-serine (DOPS) and 1,2-dioleoyl-sn-glycero-3-((N-(5-amino-1-carboxypentyl)iminodiacetic acid)succinyl) (nickel salt) (DGS-NTA-Ni<sup>2+</sup>)) were purchased from Avanti polar lipids. The first step of preparing small unilamellar vesicles (SUVs) is making DOPC, DOPS and DGS-NTA-Ni<sup>2+</sup> mixtures by dissolving them in chloroform at a ratio of 6:2:2 (w:w:w). Then, the mixed lipids were dried by a nitrogen flow and kept in a vacuum chamber overnight for further drying. The dried lipid was resuspended in measuring buffer (50 mM HEPES, pH 7.5, 100 mM KCl), followed by 30 min sonication.

### Sample preparation for HS-AFM imaging and SMFS

A 1.5-mm diameter muscovite mica sheet was glued onto a HS-AFM glass rod sample support and mounted on a HS-AFM scanner. The prepared DOPC/DOPS/DGS-NTA-Ni<sup>2+</sup> (6:2:2) SUVs were deposited on the freshly cleaved mica for around 10 min, where they formed a continuous supported lipid bilayer (SLB). The sample was then rinsed with measuring buffer (50 mM HEPES, pH 7.5, 100 mM KCl). His<sub>6</sub>-CL-CNBD constructs were carefully added in 10 μM steps while observing the sample surface with HS-AFM imaging until 2D crystals formed on the SLBs. Note, the CL-CNBD domain is a stable tetramer, and thus each CL-CNBD tetramer has four His6-tags. The unit cell dimension of the CL-CNBD tetramer is  $a = b = 11 \text{ nm}$ ,  $\gamma = 90^\circ$  (thus an area of 121 nm<sup>2</sup>) (Fig. 1g). The area occupied by a lipid molecule in a supported lipid bilayer is around 0.25 nm<sup>2</sup> (ref. 34). This suggests that there are around 480 lipid molecules under each CL-CNBD tetramer. Here, the membrane contains 20% DGS-NTA-Ni<sup>2+</sup>, that is, around 100 DGS-NTA-Ni<sup>2+</sup> lipids under each CL-CNBD tetramer, which should provide sufficient NTA-Ni<sup>2+</sup> binding sites for all accessible histidine in all four His6-tags.

Considering an unbinding force of NTA-Ni<sup>2+</sup>-His6 of 60–80 pN (ref. 35), four NTA-Ni<sup>2+</sup>-His6 bonds (further strengthened by the avidity of several bonds) should firmly immobilize the CL-CNBD tetramers for our measurements.

### HS-AFM imaging

All high-resolution images were acquired using a HS-AFM (SS-NEX, Research Institute of Biomolecule Metrology Co.) operated in tapping mode, using a laboratory-built amplitude detector<sup>36</sup>, a free amplitude and force stabilizer<sup>37</sup> and ultrashort cantilevers (8 μm) with a nominal spring constant of around 0.15 N m<sup>-1</sup>, a resonance frequency of around 600 kHz and a Q-factor of around 1.5 in liquid (USC-F1.2-k0.15, NanoWorld). Movies were recorded at imaging rates of one frame per second and at a pixel sampling of 0.5 nm per pixel.

### Functionalization of AFM tips with cAMP or cGMP

For the covalent coupling of cN to the AFM tip, a PEG molecule with two different amino-reactive groups was used: an NHS ester group that was coupled to freshly introduced amine groups on the AFM tip surface, and a slower reacting aldehyde group that coupled to the amine group of cN, thereby linking the cN to the sensor following a three-step coupling procedure. First, the AFM tips (MSNL, Bruker) were washed three times in chloroform and dried in an argon stream, and then incubated for 10 min in a 5% APTES solution in ethanol for the introduction of amine groups. After careful rinsing in ethanol, the cantilevers were incubated at 80 °C for 30 min for curing. Second, the heterobifunctional aldehyde-PEG<sub>24</sub>-NHS (Broadpharm) was attached by incubating the amine-cantilevers for 2 h in 0.5 ml chloroform containing 3.3 mg ml<sup>-1</sup> aldehyde-PEG<sub>24</sub>-NHS and 30 μl triethylamine. Third and last, the tips were rinsed with chloroform, dried with a gentle argon stream and placed on a clean flat surface (for example, a Petri dish covered with parafilm) and immersed in a 100 μl of 5 mM cAMP (or cGMP) droplet. Subsequently, 2 μl of a freshly prepared 1 M NaCNBH<sub>3</sub> solution was added and mixed carefully. After 2 h of incubation at RT, 5 μl of 1 M ethanolamine, pH 8 was added and incubated for another 10 min. The cN biosensors were then washed with measuring buffer (50 mM HEPES, pH 7.5, 100 mM KCl) and stored at 4 °C until further use (for a maximum of 3 days).

### AFM-SMFS experiments

AFM-SMFS measurements were performed using a JPK Nanowizard 4. All SMFS experiments were performed in measuring buffer (50 mM HEPES, pH 7.5, 100 mM KCl). Silicon tips with a nominal spring constant of 100 pN nm<sup>-1</sup> (MNSL, Bruker) were used for all AFM-SMFS experiments. The spring constant of the cantilevers was first carefully calibrated using JPK Nanowizard 4 based on the thermal tuning method<sup>28</sup>. Before SMFS experiments, the His<sub>6</sub>-CL-CNBD 2D crystals on the SLBs were localized by imaging. The tip was then positioned over the 2D crystal for SMFS. To generate the dynamic force spectrum, retraction velocities were varied from 0.2 μm s<sup>-1</sup> to 4.0 μm s<sup>-1</sup> after predefined cN-CNBD contact times. To obtain 2D binding kinetics, force curves were acquired at constant approach and retraction speeds of 0.2 μm s<sup>-1</sup> varying the contact duration from 0.02 s to 1.00 s. In addition, the kinetic parameters of cAMP entering a deeper binding mode (state 2 bond) were estimated quantitatively from these measurements.

### Data analysis

All AFM-SMFS data were analyzed using JPK force curve processing software (v.7.0.72). All force histograms were fitted in Origin v.2019b. The kinetic off,  $k_{\text{off}}$ , and distances to the energy barriers,  $x_{\beta}$ , of cAMP and cGMP binding with the CNBD were obtained by fitting the unbinding data with Bell-Evans<sup>22</sup>

$$F = \left( \frac{k_{\text{B}} T}{x_{\beta}} \right) \ln \frac{r x_{\beta}}{k_{\text{off}} k_{\text{B}} T} \quad (2)$$

where  $F$  is the rupture force,  $r$  is the loading rate,  $k_B$  is the Boltzmann constant and  $T$  is the absolute temperature.

The on,  $k_{\text{on}(2D)}$ , rates were obtained by fitting the binding data with probability model<sup>23</sup>. The binding frequency ( $P$ ) is related to the average number ( $n$ ) of bonds that are formed following equation (3), and  $P$  is derived directly by dividing the number of detected binding events by the total number of experimental cycles:

$$P = 1 - \exp(-n) \quad (3)$$

and considering the binding as a second-order forward and first-order reverse reaction, the relationship between the bond number ( $n$ ) and the contact time ( $t$ ) is described by equation (4):

$$n = m_r m_l A_c K_{a(2D)} [1 - \exp(1 - k_{\text{off}} t)] \quad (4)$$

where  $m_r$  (0.03 binding sites  $\text{nm}^{-2}$ ) is the 2D binding-site density derived from the CNBD tetramer 2D crystal with unit cell size of 11 nm (Fig. 1d,g),  $t$  is ligand exposure time (experimentally defined),  $m_l$  is the ligand density,  $A_c$  is the contact area between tip and sample and  $k_{\text{off}}$  is the dissociation rate derived from fitting the Bell–Evans model (equation (2)) to the dynamic force spectrum. The factor  $m_l A_c$  is set to 2, as some dual-binding force curves were detected (Extended Data Fig. 4). Therefore, the binding association constant  $K_{a(2D)}$  is the only unknown and fitted parameter.

To test whether the stronger binding mode could emerge from simultaneous rupture of several bonds, we used the Markovian model<sup>26</sup>:

$$r = k_{\text{off}} \frac{k_B T}{x_\beta} \left[ \sum_{n=1}^N \frac{1}{n^2} \exp\left(-\frac{F^* x_\beta}{n k_B T}\right) \right]^{-1} \quad (5)$$

where  $r$  is the loading rate,  $k_{\text{off}}$  and  $x_\beta$  are derived from the Bell–Evans model fit of the lower force spectrum (Fig. 5b),  $N$  is the number of bonds and  $F^*$  is the most probable unbinding force.

### MST experiments

MST experiments were performed using a Monolith NT.115 Pico (NanoTemper Technologies) and Monolith NT.115 Premium capillaries (NanoTemper Technologies). The His<sub>6</sub>-CL-CNBD complex was labeled using the Monolith Protein Labeling Kit RED-Tris-NTA, second generation. For the measurements, the concentration of labeled His<sub>6</sub>-CL-CNBD was kept constant (50 nM), and the concentration of cNs was varied from 0.00305  $\mu\text{M}$  to 100  $\mu\text{M}$ . All experiments were performed in measuring buffer (50 mM HEPES, pH 7.5, 100 mM KCl). The MST traces were analyzed using the software M.O. Affinity Analysis v.2.3 (NanoTemper Technologies).

### Setup for force probe MDS

To mimic the AFM-SMFS experiment in the force probe MDS, we simulated the entire CL-CNBD tetramer structure and connected it to a ‘substrate’ via four positional constraints on the C $\alpha$  atoms of the first residue of each monomer, mimicking the tethering of the His<sub>6</sub>-CL-CNBD construct on the Nickel–lipid bilayer in the experiment. We optimized the stiffness of the four restraints to achieve a similar orientational flexibility as expected in the experiment, thus also complying to the directional pulling forces of the cN with respect to the CNBD tetramer as estimated for the experimental setup. The cN-ligands were connected to the virtual cantilever via an explicit atomistic model of a PEG-linker around 10 nm long as used in the experiments. The cantilever was simulated by a harmonic potential with a spring constant of 100 pN  $\text{nm}^{-1}$ , also matching the experiment. Thus, moving the harmonic potential along a  $z$  axis away from the CNBD resulted in pulling the cN out of the CNBD binding pocket, while monitoring the atomic details in the cN-unbinding trajectories and the displacement of the harmonic potential reporting the force applied during the process.

### Molecular dynamics simulations

Starting cryo-EM structures of the SthK channel with bound cAMP or cGMP were obtained from the protein databank (PDB IDs: 6CJU<sup>7</sup> and 6CJT<sup>7</sup>, respectively). In the simulations only the CNBD of the protein was included, starting from residue 226, while the remaining protein residues were omitted. Missing residues and sidechains of the CNBD part were added to the structures using MODELLER<sup>38</sup> software. The partly unresolved C-helix was built in to the cryo-EM structures by aligning the C-helix residues resolved in the cryo-EM structures with the corresponding residues in the X-ray crystal structures (PDB IDs: 4D7T<sup>13</sup> and 4D7S, respectively) and, where the full C-helix was resolved, replacing the incomplete C-helix of the cryo-EM structure with the aligned full C-helix from the X-ray structure.

The general AMBER force field<sup>39</sup> parameters for the cNs (cAMP and cGMP) connected to the PEG-linker were obtained using the Antechamber package<sup>40</sup>. Atomic partial charges were obtained from restrained electrostatic potential<sup>41</sup> fit to the electrostatic potential calculated using Gaussian v.03 (ref. 42) software with Hartree–Fock theory<sup>43</sup> and 6–31G<sup>44</sup> basis set. The obtained force field parameters were converted to Gromacs format using the amb2gm script<sup>45</sup> of the AcPype<sup>46</sup> package. To allow the use of longer time steps in the MDS, virtual sites for the hydrogens of cAMP-PEG and cGMP-PEG were constructed using the MkVsites tool<sup>47</sup>.

The PEG-linker connected to the cN in each starting structure was reoriented parallel to the  $z$  axis (pulling direction) of the simulation box. One of the four binding pockets was occupied with a cN-PEG ligand in the simulations of the whole tetramer. The system was placed in a rectangular box using 1.5 nm distance to boundaries in  $x$  and  $y$  directions and given the full length of the extended ligand, around 9.5 nm, the box was set to 20 nm height in the  $z$  direction to ensure enough space for pulling out the entire cN-PEG-linker from its binding pocket. The system was solvated with TIP3P<sup>48</sup> water and 0.1 M KCl and neutralizing ions.

All MDS were performed using the GROMACS v.2020 (ref. 49) simulation package using the Amber99sb-ildn force field<sup>50</sup>. The Verlet Integrator<sup>51</sup> with a 4 fs timestep was used with virtual sites for hydrogens. The particle mesh Ewald<sup>52</sup> method was used to calculate electrostatic interactions with a cut-off length of 1 nm and a grid spacing of 0.12 nm. Van der Waals interactions were cut off at 1 nm. All bond lengths were constrained using the LINCS algorithm<sup>53</sup>. Histidine protonation states were obtained with WHATIF<sup>54</sup>, while all other amino acid protonation states were kept to their default values at pH 7.

Before the pulling simulations the systems were equilibrated with 30,000 steps steepest-descent energy minimization, followed by a three-stage equilibration procedure performed under constant pressure, constant temperature (NPT) conditions using a velocity-rescale thermostat<sup>55</sup> with a reference temperature of 298.15 K, a time constant of 0.1 ps and separate couplings for solvent (water and ions), and solute (protein and cN-PEG-linker), and the Berendsen barostat<sup>56</sup> with a reference pressure of 1 bar and a time constant of 1 ps. At the first stage, position restraints were imposed on all heavy atoms of the protein and solvent relaxation of the cN-PEG-linker was allowed during a 10 ns simulation. To avoid steric clashes originating from the initial positioning of the cN-PEG-linker, the Coulomb and van der Waals interactions of the cN-PEG-linker were initially turned off, and gradually turned on during this first stage. At the second stage, during 10 ns, the protein and cN-PEG-linker heavy-atom position restraints were gradually turned off. Flat-bottomed position restraints, designed to keep the system from detaching from its ‘substrate’ during pulling, were applied (0.3 nm flat-bottom layer thickness, force constant 100  $\text{kJ mol}^{-1}$ ) on the C $\alpha$  atoms of the monomer C-termini to mimic the effect of His<sub>6</sub>-tags used in the AFM experiment. At the third stage, the system was simulated freely under NPT conditions with the before-mentioned flat-bottomed position restraints maintained for 130 ns.

All pulling simulations were initiated from 30 snapshots obtained at even time intervals between 10 ns and 130 ns from the trajectory

of the third stage described above using the Gromacs COM pulling method. Here, a virtual cantilever, that is, a harmonic potential with a spring constant of  $100 \text{ pN nm}^{-1}$  was applied to the end of the PEG-linker and moved away from the binding pocket along the  $z$  coordinate of the simulation box using ten different velocities between  $5 \text{ m s}^{-1}$  and  $0.005 \text{ m s}^{-1}$ . Pressure coupling was not applied in the pulling ( $z$ ) direction of the box.

For each individual pulling simulation the unbinding force and loading rate were determined from the difference between an average around the maximum force and baseline after the unbinding, and from the slope of the force-time curve before the unbinding, respectively. The dynamic force spectrum was calculated from the average loading rate and rupture force for each pulling velocity (30 simulations for each pulling velocity). Kinetic parameters  $k_{\text{off}}$  rate and distance to the energy barrier  $x_{\beta}$ , of cAMP and cGMP binding with the CNBD were obtained by fitting the unbinding data with the Bell–Evans model<sup>22</sup> (equation (2)).

Hydrogen bond interaction strengths  $U(r)$  along the unbinding simulations were estimated based on donor-acceptor distances  $r_{\text{DA}}$  between the cN and the protein residues using the Espinosa formula<sup>57</sup>:

$$U(r_{\text{DA}}) = 49,100e^{-3.6r_{\text{DA}}} - 11,800e^{-2.73r_{\text{DA}}} \quad (6)$$

The strengths are reported per residue and averaged over the 30 simulations of the slowest loading rate.

The distribution of unbinding forces in the Bell–Evans model is<sup>58</sup>:

$$P(F_i) = \frac{k_{\text{off}}}{r} e^{-\frac{F_i x_{\beta}}{k_{\text{BT}}}} e^{-\frac{k_{\text{off}} k_{\text{BT}} T}{r x_{\beta}} \left(1 - e^{-\frac{F_i x_{\beta}}{k_{\text{BT}}}}\right)} \quad (7)$$

where  $F_i$  is an unbinding force,  $r$  is the loading rate,  $k_{\text{B}}$  is the Boltzmann constant,  $T$  is the absolute temperature,  $k_{\text{off}}$  is the dissociation rate constant at zero force and  $x_{\beta}$  is the distance to the unbinding barrier from the free energy minimum. To obtain the theoretical distribution of unbinding force deviations relative to the average unbinding force as shown in Extended Data Fig. 3, we sampled this distribution for loading rate and unbinding force ranges obtained from the AFM-SMFS experiment and force probe MDS.

## Reporting summary

Further information on research design is available in the Nature Portfolio Reporting Summary linked to this article.

## Data availability

The source data files contain all data (force distribution histograms, H-bond distributions) necessary to interpret, verify and extend the presented work. In the absence of dedicated data repositories for raw data AFM force curves and MDS trajectories, and in light of the instructions needed to open these files in proprietary software (in the case of the AFM force curves) and the additional information (parameters and conditions) needed to understand and use the data, raw data AFM force curves and MDS trajectories can be received from S.S. (sis2019@med.cornell.edu) and H.G. (hgrubmu@gwdg.de), respectively, upon reasonable request. Source data are provided with this paper.

## References

- Asakawa, H., Yoshioka, S., Nishimura, K.-I. & Fukuma, T. Spatial distribution of lipid headgroups and water molecules at membrane/water interfaces visualized by three-dimensional scanning force microscopy. *ACS Nano* **6**, 9013–9020 (2012).
- Koehler, M. et al. Control of ligand-binding specificity using photocleavable linkers in AFM force spectroscopy. *Nano Lett.* **20**, 4038–4042 (2020).
- Miyagi, A. & Scheuring, S. Automated force controller for amplitude modulation atomic force microscopy. *Rev. Sci. Instrum.* **87**, 053705 (2016).

- Miyagi, A. & Scheuring, S. A novel phase-shift-based amplitude detector for a high-speed atomic force microscope. *Rev. Sci. Instrum.* **89**, 083704 (2018).
- Sali, A. & Blundell, T. L. Comparative protein modelling by satisfaction of spatial restraints. *J. Mol. Biol.* **234**, 779–815 (1993).
- Wang, J., Wolf, R. M., Caldwell, J. W., Kollman, P. A. & Case, D. A. Development and testing of a general amber force field. *J. Comput. Chem.* **25**, 1157–1174 (2004).
- Wang, J., Wang, W., Kollman, P. A. & Case, D. A. Automatic atom type and bond type perception in molecular mechanical calculations. *J. Mol. Graph Model* **25**, 247–260 (2006).
- Bayly, C. I. et al. A well-behaved electrostatic potential based method using charge restraints for deriving atomic charges: the RESP model. *J. Phys. Chem.* **97**, 10269–10280 (1993).
- Frisch, M. J. et al. Gaussian v.3, Revision C.02 (Gaussian, Inc., 2004).
- Roothaan, C. C. J. New developments in molecular orbital theory. *Rev. Mod. Phys.* **23**, 69–89 (1951).
- Rassolov, V. A., Pople, J. A., Ratner, M. A. & Windus, T. L. 6-31G\* basis set for atoms K through Zn. *J. Chem. Phys.* **109**, 1223–1229 (1998).
- Mobley, D. L., Chodera, J. D. & Dill, K. A. On the use of orientational restraints and symmetry corrections in alchemical free energy calculations. *J. Chem. Phys.* **125**, 084902–084902 (2006).
- Sousa da Silva, A. W. & Vranken, W. F. ACPYPE—AnteChamber Python Parser interface. *BMC Res. Notes* **5**, 367 (2012).
- Larsson, P., Kneiszl, R. C. & Marklund, E. G. MkVsites: a tool for creating GROMACS virtual sites parameters to increase performance in all-atom molecular dynamics simulations. *J. Comput. Chem.* **41**, 1564–1569 (2020).
- Jorgensen, W. L., Chandrasekhar, J., Madura, J. D., Impey, R. W. & Klein, M. L. Comparison of simple potential functions for simulating liquid water. *J. Chem. Phys.* **79**, 926–935 (1983).
- Abraham, M. J. et al. GROMACS: high performance molecular simulations through multi-level parallelism from laptops to supercomputers. *SoftwareX* **1–2**, 19–25 (2015).
- Verlet, L. Computer ‘experiments’ on classical fluids. I. Thermodynamical properties of Lennard-Jones molecules. *Phys. Rev.* **159**, 98–103 (1967).
- Lindorff-Larsen, K. et al. Improved side-chain torsion potentials for the Amber ff99SB protein force field. *Proteins* **78**, 1950–1958 (2010).
- Darden, T., York, D. & Pedersen, L. Particle mesh Ewald: an  $N$ -log( $N$ ) method for Ewald sums in large systems. *J. Chem. Phys.* **98**, 10089–10092 (1993).
- Hess, B., Bekker, H., Berendsen, H. J. C. & Fraaije, J. G. E. M. LINCS: a linear constraint solver for molecular simulations. *J. Comput. Chem.* **18**, 1463–1472 (1997).
- Vriend, G. WHAT IF: a molecular modeling and drug design program. *J. Mol. Graph* **8**, 52–56 (1990).
- Bussi, G., Donadio, D. & Parrinello, M. Canonical sampling through velocity rescaling. *J. Chem. Phys.* **126**, 014101 (2007).
- Berendsen, H. J. C., Postma, J. P. M., Gunsteren, W. F. V., DiNola, A. & Haak, J. R. Molecular dynamics with coupling to an external bath. *J. Chem. Phys.* **81**, 3684–3690 (1984).
- Espinosa, E. & Molins, E. Retrieving interaction potentials from the topology of the electron density distribution: the case of hydrogen bonds. *J. Chem. Phys.* **113**, 5686–5694 (2000).
- Evans, E. Probing the relation between force—lifetime—and chemistry in single molecular bonds. *Annu. Rev. Biophys. Biomol. Struct.* **30**, 105–128 (2001).

## Acknowledgements

We thank M. Rangl for initial experiments. Work in the Scheuring laboratory was supported by grants from the National Institute of Health, National Center for Complementary and Integrative Health DP1AT010874 and National Institute of Neurological Disorders and Stroke

R01NS110790, and by the Kavli Institute at Cornell. Work in the Nimigean laboratory was supported by the National Institute of Health (GM124451 to C.M.N.) and the American Heart Association (18POST33960309 to P.A.M.S.). Work in the Grubmüller laboratory was funded by the Max Planck Society and by the German Science Foundation (DFG), Excellence Strategy Grant MBExC 2067/1-390729940; computer time was provided by the Max Planck Computing and Data Facility. A.C.V. was additionally supported by the European Union's Horizon 2020 Framework Programme for Research and Innovation, Specific Grant Agreement No. 945539 (Human Brain Project SGA3).

### Author contributions

Y.P., C.M.N. and S.S. designed the experiments. P.A.M.S. expressed and purified the protein. Y.P. performed HS-AFM and AFM-SMFS experiments. Y.P. did the HS-AFM and AFM-SMFS data analysis. E.P., A.C.V. and H.G. performed and analyzed force probe MDS. Y.P., E.P., H.G. and S.S. wrote the paper. All authors edited the paper.

### Competing interests

The authors declare no competing interests.

### Additional information

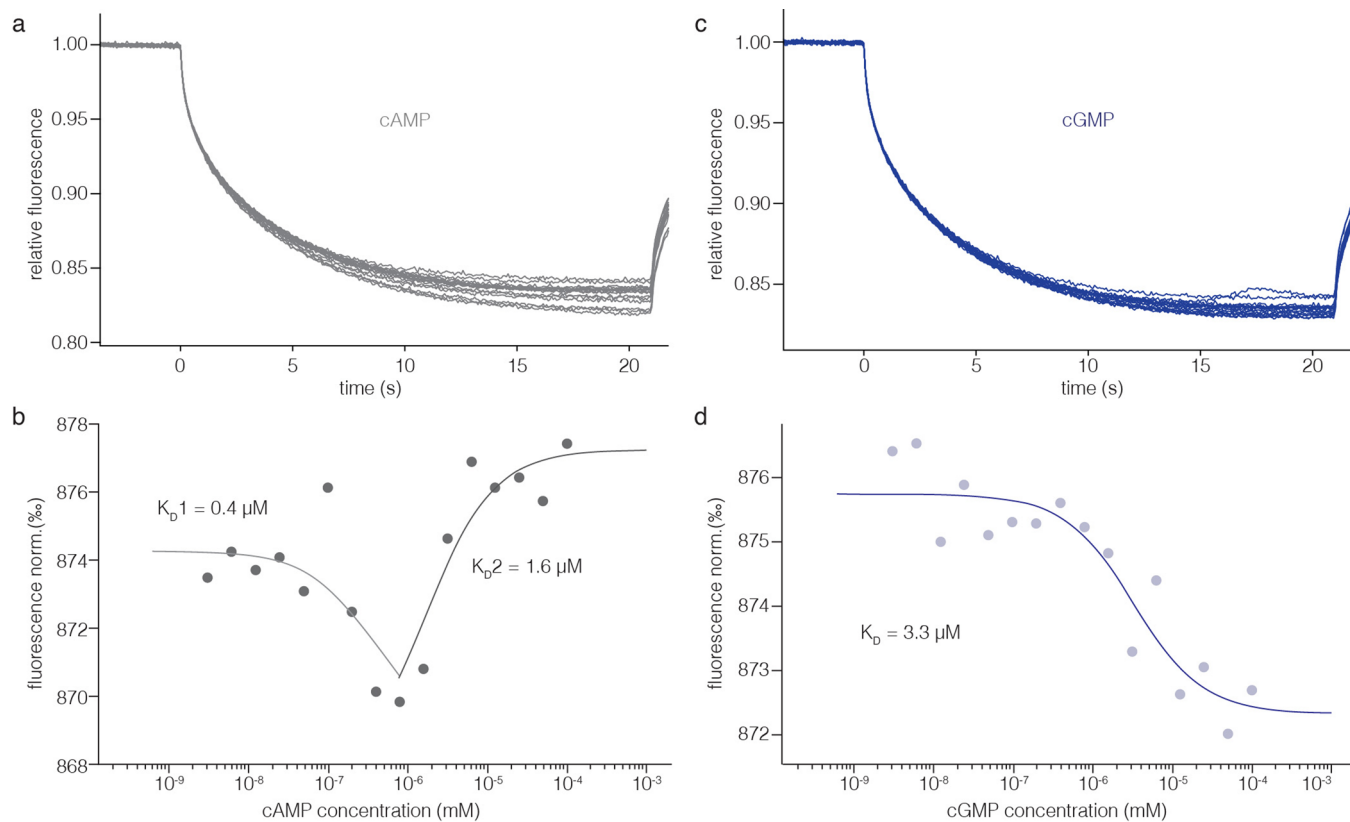
**Extended data** is available for this paper at <https://doi.org/10.1038/s41594-023-00955-3>.

**Supplementary information** The online version contains supplementary material available at <https://doi.org/10.1038/s41594-023-00955-3>.

**Correspondence and requests for materials** should be addressed to Simon Scheuring.

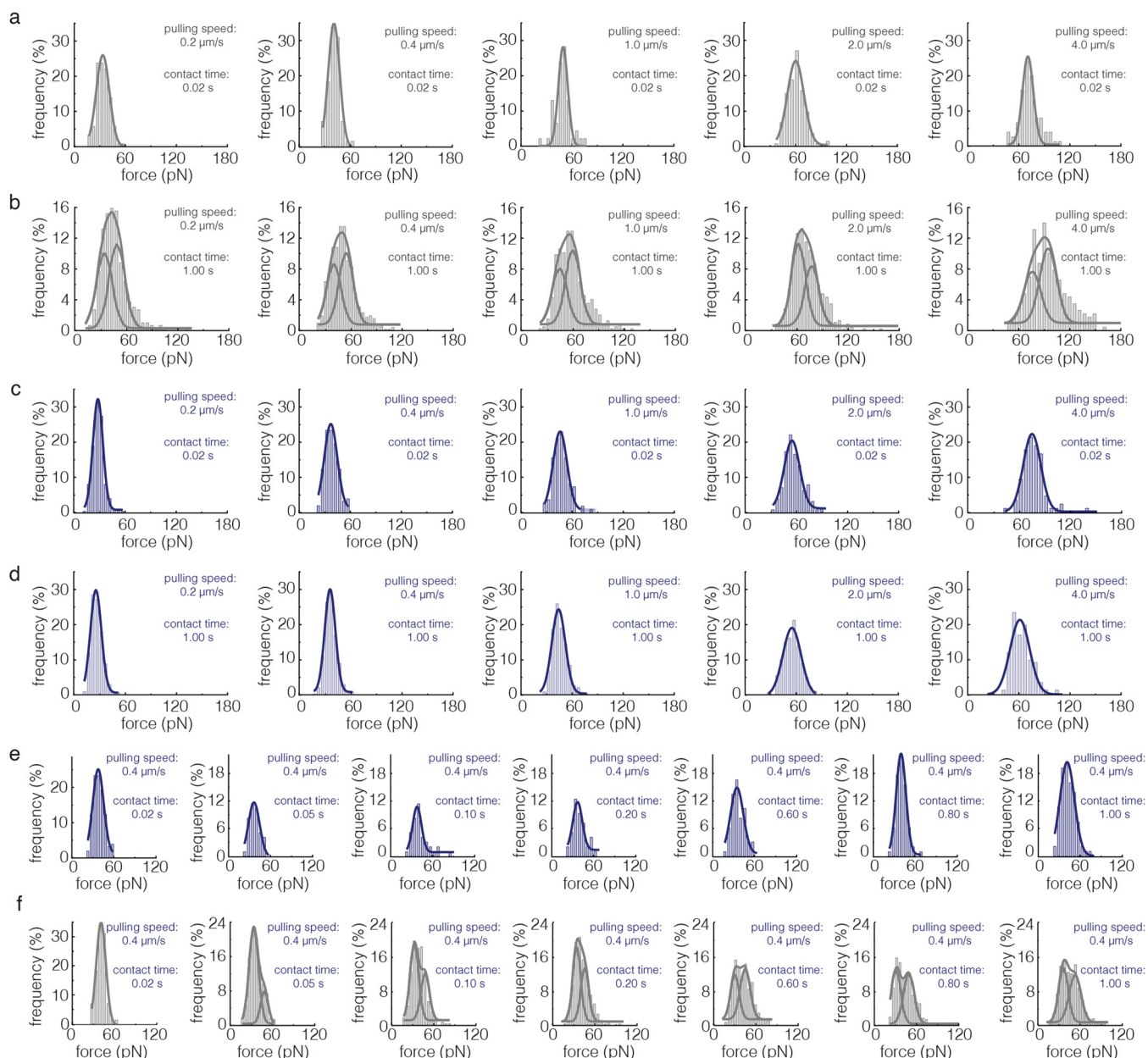
**Peer review information** *Nature Structural & Molecular Biology* thanks Baron Chanda and the other, anonymous, reviewer(s) for their contribution to the peer review of this work. Peer reviewer reports are available. Primary Handling Editors: Florian Ullrich and Katarzyna Ciazynska, in collaboration with the *Nature Structural & Molecular Biology* team.

**Reprints and permissions information** is available at [www.nature.com/reprints](http://www.nature.com/reprints).



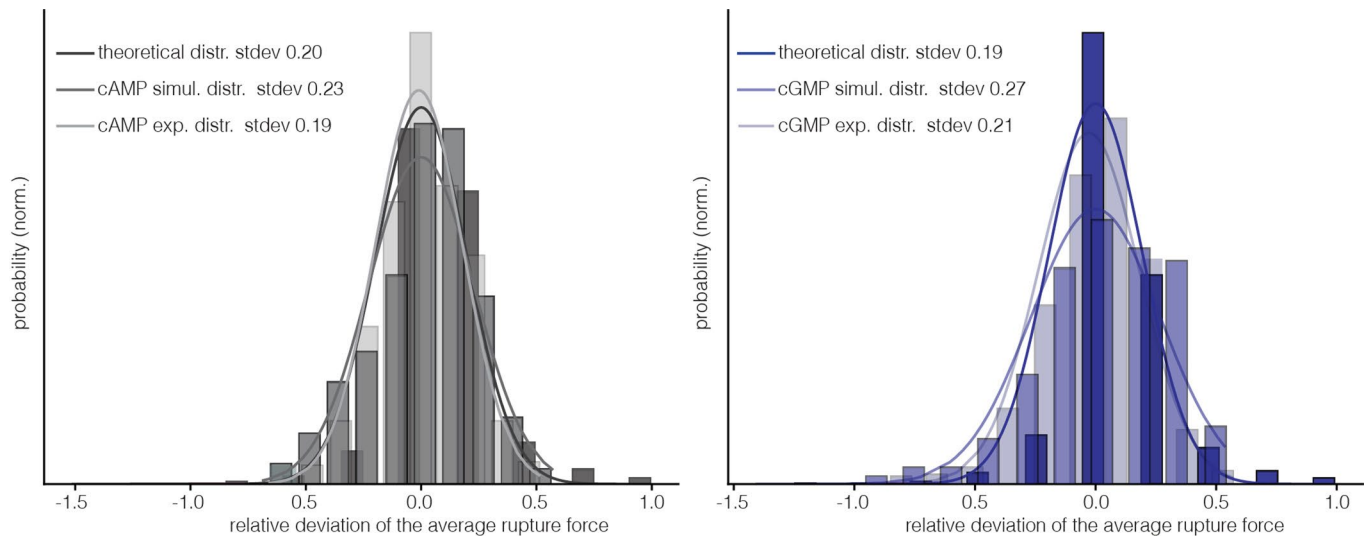
**Extended Data Fig. 1 | cNs-CNBD binding studies using microscale thermophoresis (MST). a** and **c**) Microscale thermophoresis (MST) traces of cAMP-CNBD (a) and cGMP-CNBD (c) interactions, respectively. **b**) Binding curve of labeled CNBD with cAMP. Two binding phases were detected. The first had

a  $K_D$  of  $0.4 \pm 0.5 \mu\text{M}$ , and the second had a  $K_D$  of  $1.6 \pm 1.1 \mu\text{M}$ . **d**) Binding curve of labeled CNBD with cGMP. The  $K_D$  value of cGMP-CNBD was  $3.3 \pm 1.8 \mu\text{M}$ . The concentration of labeled His<sub>6</sub>-C-linker-CNBD was kept constant (50 nM), and the concentration of cNs was varied from 0.00305  $\mu\text{M}$  to 100  $\mu\text{M}$ .

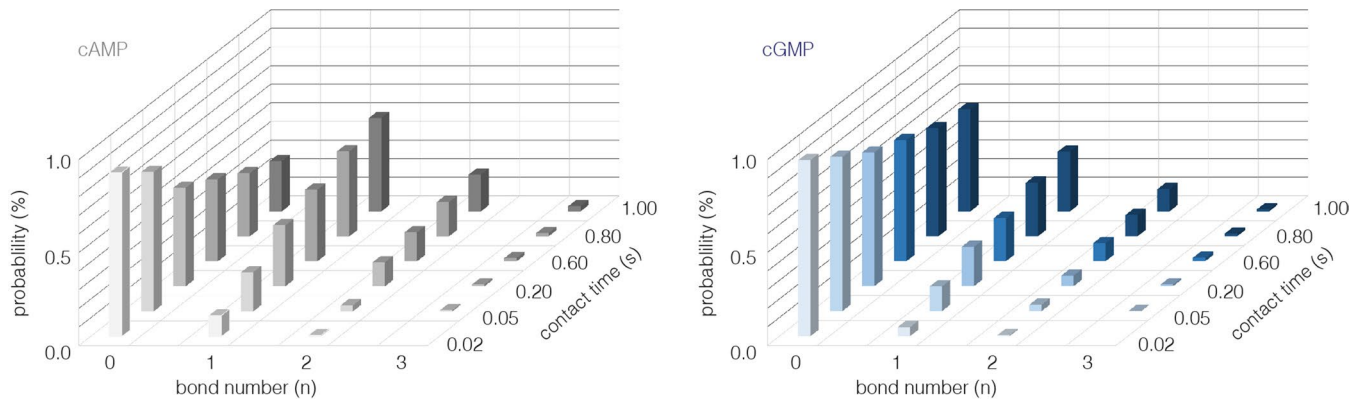


**Extended Data Fig. 2 | Distributions of rupture forces of cAMP-CNBD or cGMP-CNBD bonds under various conditions.** **a**) Force distribution of cAMP-CNBD unbinding following 0.02 s bond formation at varying pulling velocity (top right in each graph). **b**) Force distribution of cAMP-CNBD unbinding following 1.00 s bond formation at varying pulling velocities (top right in each graph). The force distributions are fitted with bimodal Gaussian fits to extract the most probable rupture forces for binding state 1 (first peak) and binding state 2 (second peak), which are then used for Bell–Evans model fitting. **c**) Force

distribution of cGMP-CNBD unbinding following 0.02 s bond formation at varying pulling velocities (top right in each graph). **d**) Force distribution of cGMP-CNBD unbinding following 1.00 s bond formation at varying pulling velocities (top right in each graph). **e**) and **f**) Distributions of rupture forces of cGMP-CNBD (**e**) and cAMP-CNBD (**f**) unbinding following different bond formation times and at 0.4  $\mu\text{m/s}$  pulling velocity). Bimodal Gaussian fits are used to extract the number of events for each bond state, which is then used to calculate the probability of occurrence of binding state 2.

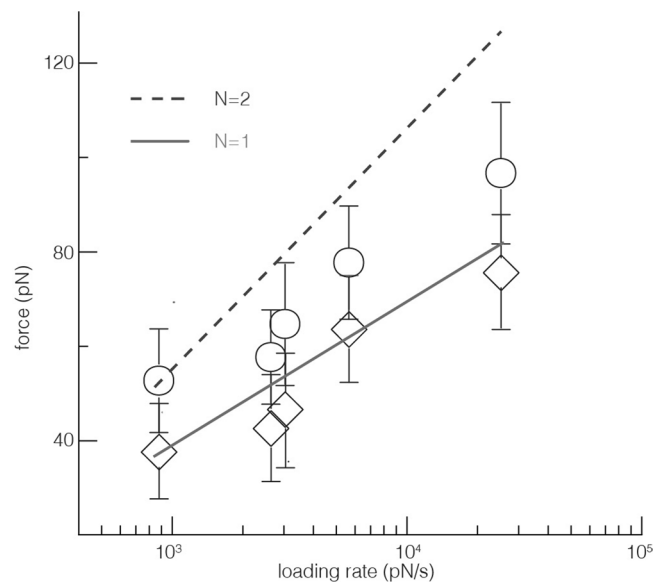


**Extended Data Fig. 3 | Deviations of rupture force distributions.** Theoretical, simulation and experimental unbinding force distributions (normalized by loading rates) of cAMP (left) and cGMP (right). The experimental unbinding force distributions are the distributions after 0.02 s bond formation time.



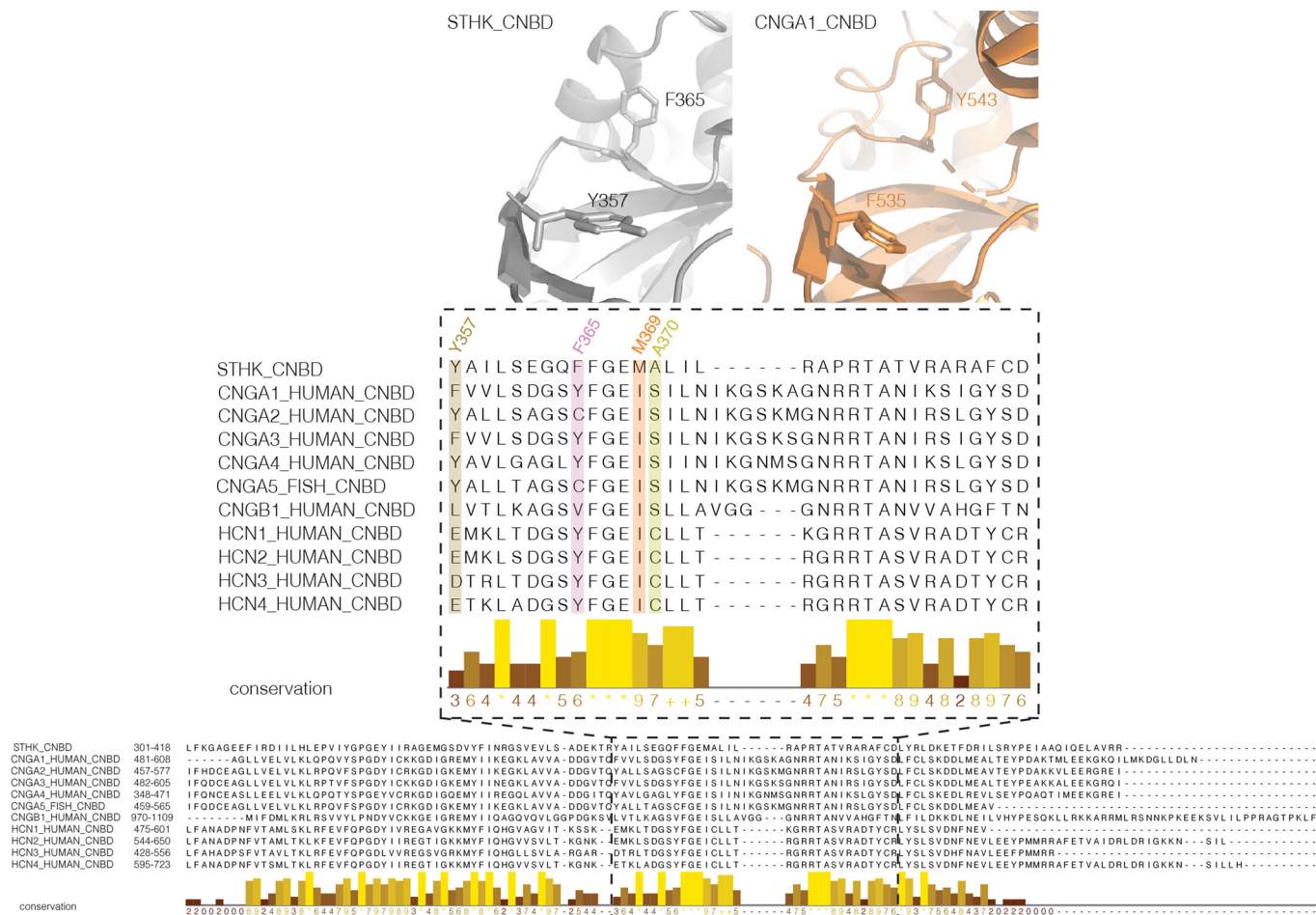
**Extended Data Fig. 4 | Number of bond ruptures as a function of bond-formation time for cAMP-CNBD (left) and cGMP-CNBD (right).** With increasing cN contact time, the frequency of unsuccessful (0 bond) force-distance cycles

decreases, while the number of successful (1 bond) force-distance cycles increases. Concomitantly, a fraction of force-distance cycles reported multiple (2 or 3) binding events.



**Extended Data Fig. 5 | Markovian sequence analysis for the force spectroscopy experiments of cAMP-CNBD at 1 s contact time.** Markovian model fitting for 1 (gray line) and 2 (dashed line) bonds.  $k_{off}$  and  $x_{\beta}$  values were derived from the Bell-Evans model fit to the canonical binding mode

(see Fig. 5b). The most probable rupture force (Gaussian peak) and error (full width at half maximum of the Gaussian peak) at each loading rate was determined through Gaussian fitting of the corresponding histogram (total data points for all histograms,  $N = 1898$ , Extended Data Fig. 2b).



**Extended Data Fig. 6 | Comparison of SthK with CNG and HCN channels, with a focus on their cN binding pockets.** Top: cNs binding pocket of SthK (left, gray) and CNGA1 (right, orange) showing that the residues Y and F are swapped in CNGA1 channels compared with SthK. Bottom: Sequence alignment of SthK

with CNG and HCN channels showing that Y357 and F365 identified by MDS to be crucial in cN discrimination in SthK are not conserved, whereas M369 is a conservative mutation and A370 is a semi-conservative mutation. cAMP interacts with Y357, M369 and A370, and cGMP interacts with F365.

## Reporting Summary

Nature Portfolio wishes to improve the reproducibility of the work that we publish. This form provides structure for consistency and transparency in reporting. For further information on Nature Portfolio policies, see our [Editorial Policies](#) and the [Editorial Policy Checklist](#).

### Statistics

For all statistical analyses, confirm that the following items are present in the figure legend, table legend, main text, or Methods section.

- | n/a                                 | Confirmed  |
|-------------------------------------|--|
| <input type="checkbox"/>            | <input checked="" type="checkbox"/> The exact sample size ( $n$ ) for each experimental group/condition, given as a discrete number and unit of measurement  |
| <input type="checkbox"/>            | <input checked="" type="checkbox"/> A statement on whether measurements were taken from distinct samples or whether the same sample was measured repeatedly  |
| <input type="checkbox"/>            | <input checked="" type="checkbox"/> The statistical test(s) used AND whether they are one- or two-sided<br><i>Only common tests should be described solely by name; describe more complex techniques in the Methods section.</i>   |
| <input checked="" type="checkbox"/> | <input type="checkbox"/> A description of all covariates tested  |
| <input checked="" type="checkbox"/> | <input type="checkbox"/> A description of any assumptions or corrections, such as tests of normality and adjustment for multiple comparisons   |
| <input type="checkbox"/>            | <input checked="" type="checkbox"/> A full description of the statistical parameters including central tendency (e.g. means) or other basic estimates (e.g. regression coefficient) AND variation (e.g. standard deviation) or associated estimates of uncertainty (e.g. confidence intervals) |
| <input type="checkbox"/>            | <input checked="" type="checkbox"/> For null hypothesis testing, the test statistic (e.g. $F$ , $t$ , $r$ ) with confidence intervals, effect sizes, degrees of freedom and $P$ value noted<br><i>Give <math>P</math> values as exact values whenever suitable.</i>                            |
| <input checked="" type="checkbox"/> | <input type="checkbox"/> For Bayesian analysis, information on the choice of priors and Markov chain Monte Carlo settings  |
| <input checked="" type="checkbox"/> | <input type="checkbox"/> For hierarchical and complex designs, identification of the appropriate level for tests and full reporting of outcomes  |
| <input checked="" type="checkbox"/> | <input type="checkbox"/> Estimates of effect sizes (e.g. Cohen's $d$ , Pearson's $r$ ), indicating how they were calculated  |

*Our web collection on [statistics for biologists](#) contains articles on many of the points above.*

### Software and code

Policy information about [availability of computer code](#)

- |                 |   |
|-----------------|---|
| Data collection | All high-resolution images were collected using a HS-AFM (SS-NEX, Research Institute of Biomolecule Metrology Co.). The AFM-SMFS measurements were collected using a JPK Nanowizard 4. All MDS were performed using the GROMACS2020 simulation package using the Amber99sb-ildn force field. MST experiments were performed using a Monolith NT.115 Pico (NanoTemper Technologies, Germany) and Monolith NT.115 Premium capillaries (NanoTemper Technologies, Germany). |
| Data analysis   | All AFM-SMFS data were analyzed by using JPK force curve processing software (7.0.72). All force histograms were fitted in Origin 2019b. The MST traces were analyzed using the software M.O. Affinity Analysis v2.3 (NanoTemper Technologies, Germany).  |

For manuscripts utilizing custom algorithms or software that are central to the research but not yet described in published literature, software must be made available to editors and reviewers. We strongly encourage code deposition in a community repository (e.g. GitHub). See the Nature Portfolio [guidelines for submitting code & software](#) for further information.

## Data

Policy information about [availability of data](#)

All manuscripts must include a [data availability statement](#). This statement should provide the following information, where applicable:

- Accession codes, unique identifiers, or web links for publicly available datasets
- A description of any restrictions on data availability
- For clinical datasets or third party data, please ensure that the statement adheres to our [policy](#)

The source data files contain all data (force distribution histograms, H-bond distributions) necessary to interpret, verify and extend the presented work. In the absence of dedicated data repositories for raw data AFM force curves and MDS trajectories, and in light of the instructions needed to open these files in proprietary software (in the case of the AFM force curves) and the additional information (parameters and conditions) needed to understand and use the data, raw data AFM force curves and MDS trajectories can be received from Simon Scheuring (sis2019@med.cornell.edu) and Helmut Grubmüller (hgrubmu@gwdg.de), respectively, upon reasonable request.

## Human research participants

Policy information about [studies involving human research participants and Sex and Gender in Research](#).

Reporting on sex and gender	N/A
Population characteristics	N/A
Recruitment	N/A
Ethics oversight	N/A

Note that full information on the approval of the study protocol must also be provided in the manuscript.

## Field-specific reporting

Please select the one below that is the best fit for your research. If you are not sure, read the appropriate sections before making your selection.

- Life sciences       Behavioural & social sciences       Ecological, evolutionary & environmental sciences

For a reference copy of the document with all sections, see [nature.com/documents/nr-reporting-summary-flat.pdf](https://nature.com/documents/nr-reporting-summary-flat.pdf)

## Life sciences study design

All studies must disclose on these points even when the disclosure is negative.

Sample size	No statistical methods were used to determine the sample size. Sample size was determined based on the amount that is sufficient for the histograms creating and Gaussian fitting applied in this study. For each pulling speed or different contact time, at least 38 events were used for the histogram creating and Gaussian fitting (in most cases above hundred events).
Data exclusions	No data exclusions were made.
Replication	All the experiments were replicated 2-3 times.
Randomization	For AFM-SMFS experiments, force distance curves at different pulling speed were collected from multiple random areas. For high resolution AFM imaging experiments, multiple areas were randomly acquired. As the CNBD molecules formed uniform 2D crystal in our experiments, we didn't allocate experimental groups.
Blinding	No blinding was required for single molecule biophysics research. We did quantitative analysis of our collected data. For the data analysis, we used the commercial JPK data processing software (7.0.72). All the data were analyzed in the same software and using the same criteria.

## Reporting for specific materials, systems and methods

We require information from authors about some types of materials, experimental systems and methods used in many studies. Here, indicate whether each material, system or method listed is relevant to your study. If you are not sure if a list item applies to your research, read the appropriate section before selecting a response.

## Materials & experimental systems

n/a	Involvement in the study
<input checked="" type="checkbox"/>	<input type="checkbox"/> Antibodies
<input checked="" type="checkbox"/>	<input type="checkbox"/> Eukaryotic cell lines
<input checked="" type="checkbox"/>	<input type="checkbox"/> Palaeontology and archaeology
<input checked="" type="checkbox"/>	<input type="checkbox"/> Animals and other organisms
<input checked="" type="checkbox"/>	<input type="checkbox"/> Clinical data
<input checked="" type="checkbox"/>	<input type="checkbox"/> Dual use research of concern

## Methods

n/a	Involvement in the study
<input checked="" type="checkbox"/>	<input type="checkbox"/> ChIP-seq
<input checked="" type="checkbox"/>	<input type="checkbox"/> Flow cytometry
<input checked="" type="checkbox"/>	<input type="checkbox"/> MRI-based neuroimaging